Old Dominion University

ODU Digital Commons

Field Emission Studies Toward Improving the Performance of DC High Voltage Photoelectron Guns

Mahzad BastaniNejad
Old Dominion University

Recommended Citation

FIELD EMISSION STUDIES

TOWARD IMPROVING THE PERFORMANCE OF

DC HIGH VOLTAGE PHOTOELECTRON GUNS

by

Mahzad BastaniNejad
B.S. July 2000, Shiraz University, Iran
M.S. April 2004, Clarkson University, Potsdam NY

A Thesis Submitted to the Faculty of
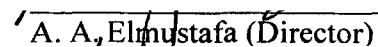Old Dominion University in Partial Fulfillment of the
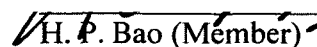Requirements for the Degree of

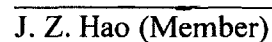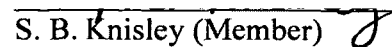DOCTOR OF PHILOSOPHY

MECHANICAL ENGINEERING

OLD DOMINION UNIVERSITY
August 2013

Approved by:

A. A. Elmustafa (Director)

H. P. Bao (Member)

J. Z. Hao (Member)

S. B. Knisley (Member)

ABSTRACT

FIELD EMISSION STUDIES TOWARD IMPROVING THE PERFORMANCE OF DC HIGH VOLTAGE PHOTOELECTRON GUNS

Mahzad BastaniNejad
Old Dominion University, 2012
Director: A.A. Elmustafa

Field emission is the main mechanism that prevents DC high voltage photoemission electron guns from operating at the very high bias voltages required to produce low emittance beams. Gas conditioning is shown to eliminate field emission from cathode electrodes used inside DC high voltage photoelectron guns. Measurements and simulation results indicate that gas conditioning eliminates field emission from cathode electrodes via two mechanisms: sputtering and implantation, with the benefits of implantation reversed by heating the electrode. The field emission characteristics of 5 stainless steel electrodes varied significantly upon the initial application of voltage but improved to nearly the same level after helium and krypton gas conditioning, exhibiting less than 10 pA field emission at - 225kV bias voltage with a 50 mm cathode/anode gap, corresponding to a field strength ~ 13 MV/m. Field emission could be reduced with either krypton or helium, but there were conditions related to gas choice, voltage and field strength that were more favorable than others.

The field emission characteristics of niobium electrodes were compared to those of stainless steel electrodes using a DC high voltage field emission test apparatus. Out of 8 electrodes (6 niobium and 2 stainless steel), the best niobium electrode performed better than the best stainless steel electrodes. Large grain niobium exhibited no measurable field emission (< 10 pA) at 225 kV with 20 mm cathode/anode gap, corresponding to a field strength of 18.7 MV/m. Surface evaluation of all electrodes suggested no correlation between the surface roughness and the field emission current.

Removing surface particulate contaminations and protrusions using an effective

polishing and cleaning technique helps to prevent field emission. Mechanical polishing using silicon carbide paper and diamond paste is a common method of obtaining a mirror like surface finish on the cathode electrodes. However, it sometimes results rolled-over tips and embedded contamination. A different polishing technique was considered: electropolishing. Three stainless steel cathode electrodes with different initial surface roughness were electropolished by a commercial vendor, and evaluated inside a high voltage test stand. They exhibited less field emission than the diamond paste polished electrodes at the initial application of high voltage; but they were less receptive to ion implantation, which is a beneficial aspect of gas conditioning that serves to increase the work function of the cathode surface. Ultimately, the electropolished electrodes exhibited more field emission than diamond-paste polished electrodes.

This thesis is dedicated to my husband, Alireza Mazaheri, and to my parents who were true loving support in every step of my education.

ACKNOWLEDGMENTS

TABLE OF CONTENTS

LIST OF TABLES

LIST OF FIGURES

CHAPTER 1

INTRODUCTION

Field emission is the primary mechanism that limits the maximum achievable bias voltage, and therefore the electron beam energy of DC high voltage photoemission electron guns [1-3]. Low level field emission from the cathode electrode serves to degrade the vacuum which in turn reduces the photocathode lifetime due to ion bombardment [4-7]. High levels of field emission can damage photogun components, in particular the high voltage insulator.

Many accelerator applications require photoguns operating at ~ 500kV bias voltage for producing low emittance beams, comprised of a train of electron bunches [8, 9]. The beam emittance degrades in the first few centimeters of acceleration due to space charge forces within the electron bunch (Coulomb repulsion). However, space charge forces decrease with the beam energy, hence the desire to operate photoguns at the maximum possible voltage. Unfortunately and without exception, efforts to operate photoguns at 500kV and maximum field strength greater than 10 MV/m have met with problems due to field emission. To date, most publications reference beam production at bias voltage less than 400kV [10-14].

Groups working on energy recovery linac projects have been at the forefront of efforts to construct very high voltage photoguns. The photoguns at Jefferson Laboratory's Free Electron Laser [15, 16] and Daresbury Energy Recovery Linac Prototype [17, 18] use stainless steel electrodes polished to mirror-like finish using diamond grit. The Cornell University group uses electropolished stainless steel electrodes [19, 20] and groups in Japan rely on titanium cathode electrodes mechanically polished with a buffing wheel [21, 22, 23]. The cathode/anode gaps in these photoguns are typically ~ 100 mm with the intention of keeping field strength below 10 MV/m, although higher field strengths are sometimes reached at photogun locations associated with the cathode electrode support structure.

Field emission was first observed by R.W. Wood [24] in 1897. In 1923, Schottky [25] tried to explain the phenomena using classical theory, however he found that field

emission occurs at fields 10-50 times lower than what he predicted.

These early investigations revealed that field emission originates from locations on the electrodes where the work function is lower. These regions of low work function can occur at micro-structures on the electrode surface [25] or as a result of micro-particles and chemical contamination. In 1926, Millikan and Lauritsen [26] discovered that the pre-breakdown field emission current has a well defined relationship with applied field strength E, namely the log[I] varies linearly with 1/E, and that the slope of the data plotted in this manner provides a means to estimate the field enhancement factor (β) and area of the field emitter (A_e).

In 1928, Fowler and Nordheim [27] successfully established a theory of field emission whereby electrons tunnel through the surface potential barrier created by the bias voltage. Their theory presented the accurate dependence of the field emission current on electric field and work function of the surface.

The F-N theory was verified experimentally by Muller (1936) [28, 29] and Haefer (1940) [33] by building a field emission microscope and using a transmission electron microscope (TEM) to estimate the tip radius and size of the emitters. For the first time they showed that, field emission starts at about 3 GV/m for clean tungsten tips. However, when using larger electrodes (cm^2), field emission initiated at much lower fields strengths: 100 times lower than the theory [34]. It became clear that the field strength at localized regions of the broad-area electrode was enhanced. Different mechanisms were proposed to explain field enhancement but only the micro-protrusion model was confirmed by researchers [32, 33, 34].

Field emission is also an important limitation for superconducting radio frequency accelerating cavities. When the accelerating gradient reaches ~ 30 MV/m, the surface field strength is roughly twice as large. Presently, field emission limits the accelerating gradient to about 20 MV/m [35].

Much work has been devoted to improving the performance of superconducting radio frequency accelerating cavities. Research indicates that micron and sub-micron particulate contamination on the surface of the cavity is the source of pre-breakdown field emission [36-39]. It was found that the number of emission sites depends on preparatory surface treatment and the handling of parts during cavity construction. Vast

effort was expended in order to set up procedures for preparing and cleaning the surfaces. For example, high pressure water rinse (HPR) and vacuum high-temperature degassing have been shown to improve the performance of cavities, achieving accelerating gradients in excess of 30MV/m [40].

For DC high voltage guns, strategies to reduce field emission and protect the high voltage insulator are being actively pursued at many laboratories. Large dimensions help reduce the field strength at some locations within the photogun but can introduce considerable expense when insulator flanges exceed 13 inches in diameter. Large dimensions also make it more difficult to achieve ultrahigh vacuum. An inverted gun design [41] reduces the amount of metal biased at high voltage, and if field emission occurs, the electrons are less likely to strike the insulator due to the orientation of the electrostatic field lines. Segmented insulators [42] successfully shield the insulator from field emission and a recent demonstration indicates successful operation at 500 kV [49]. Field emission coatings [44] once seemed promising but unfortunately, serve to trap gas which is liberated during high voltage processing. All of these approaches are reasonable to pursue, however, it is best to prevent field emission altogether.

Furuta et al. [45] demonstrated that a molybdenum cathode and titanium anode were superior to stainless steel electrodes, exhibiting less than 1 nA field emission at field strength >100 MV/m; however, all of these measurements were performed at relatively low voltage and with small cathode/anode gaps. Similar reports can be found in literature for electrodes exhibiting small amounts of field emission at very high field strength [46], however photogun groups encounter problematic field emission at 10 MV/m or lower. The disparity between the encouraging results with small gaps and disappointing results obtained with actual photoguns indicates that field emission studies must be carried out using a test apparatus that closely resembles the actual photogun.

The main objectives of this work were to find the electrode materials that exhibit low levels of field emission, to study gas conditioning as a means to eliminate field emission once the photogun has been constructed, and to study polishing techniques that reliably minimize field emission from cathodes inside DC high voltage guns. The final chapter describes Fowler-Nordheim behavior of metallic breakdown from RF cavities.

CHAPTER 2

THEORETHICAL BACKGROUND

Fowler and Nordheim [47] were the first to assert that field emission was a quantum mechanical process, with electrons tunneling through the potential barrier in high electric field (>100 MV/m). The F-N theory very accurately predicted the onset of field emission from single emitters however it took many more years to modify the F-N theory to explain field emission from broad area cathode surfaces [48]. Eventually, it became clear that field emission was a complicated process, with many relevant factors to consider including, micro-protrusions, contamination, localized vacuum conditions, ionization of the desorbed gas and ion exchange processes from the contaminated areas on the metallic surface.

2.1 FOWLER – NORDHEIM THEORY OF FIELD EMISSION

The diagram in Fig. 2.1.1 is a common representation of electrons tunneling through a modified barrier in the presence of high electric field. When the electric field is not present, the energy of electrons is not high enough to overcome the potential barrier and leave the material. In the presence of the electric field, the barrier is lowered (Schottky Effect), however the electron energy is still too low. Fowler and Nordheim proposed that electrons tunnel through the barrier, with the presence of the electric field serving to create a narrow "triangle", which increases the likelihood of tunneling taking place. The width of the triangular-shaped potential barrier is defined by the work function, the image charge and the external applied electric field as the eq. 1:

$$V(x) = E_{vac} - eEx - \frac{1}{4\pi\varepsilon_0} \frac{E^2}{4x} \qquad \text{(eq. 1)}$$

where E_{vac} is the energy of vacuum, e is electron's charge, E is external applied electric field and coordinate x is shown on the following Figure:
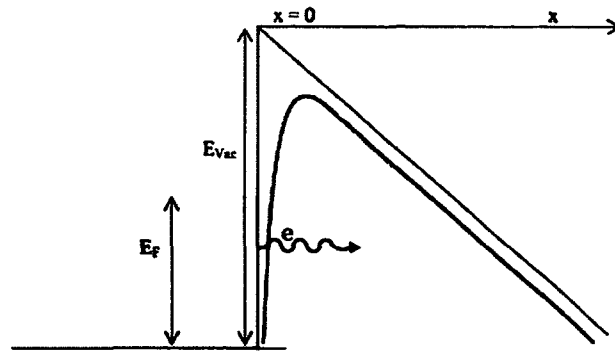
Fig. 2.1.1. Electron Tunneling

The derivation of Fowler-Nordheim expression includes three important mathematical steps. At first, the electron supply function $N(w_x)dw_x$ is obtained which gives the rate of incident electrons on the barrier from inside the metal. The next step is to calculate the probability of transit of an electron with energy of wx through the barrier. Therefore the total number of electrons with energies between wx and wx+dwx that tunnel through the barrier is:

$$J_F = e \int_{All\ Energies} D(W_x)N(W_x)dW \qquad (eq.\ 2)$$

After solving these equations, the classic formulation for Fowler Nordheim is expressed as the following:

$$J_{OF} = \frac{1.54\times10^{-6}\ E^2}{\phi\ t^2(y)} \exp\left[\frac{-6.83\times10^9\ \phi^{1.5}v(y)}{E}\right] \qquad (eq.\ 3)$$

where J_{OF} is the field emission current density, E is surface electric field(Vm-1), ϕ the work function of emitting surface (ev), t(y) and v(y) are tabulated dimensionless elliptic functions [A-C] of the parameter y which is defined by

$$y = 3.79 \times 10^{-5} \; E^{\frac{1}{2}}/\phi \qquad \text{(eq. 4)}$$

t(y) is a very slowly varying function of y that can be taken as unity for the usual high fields occur at the tip of emission sites like $3 \times 10^9 \lesssim E \lesssim 10^{10}$ v/m. v(y) however shows a field dependence behavior for the range of $2 \times 10^9 \lesssim E \lesssim 5 \times 10^{10}$ v/m , it can be approximated as the following [49]

$$v(y) = 0.956 - 1.062 \, y^2 \qquad \text{(eq. 5)}$$

For the field to be applied on an emission area of A_e , the emission current i_{OF} from this region will be

$$I_{OF} = J_{OF} \, A_e \qquad \text{(eq. 6)}$$

After substituting for t(y) and v(y) and rewriting the equations in the logarithmic form, we will have

$$\text{Log} \, \frac{i_{oF}}{E^2} = \text{Log} \left[1.54 \times 10^{-6} \, A_e . \frac{10^{4.52\Phi^{-1/2}}}{\Phi} \right] - 2.84 \times 10^9 \Phi^{1.5} . \frac{1}{E} \qquad \text{(eq. 7)}$$

If the value of E is known, the plot of $Log(I/E^2)$ versus $(1/E)$ is a line with the following slope and intercept equation:
slope:

$$\frac{d(\log i_{oF}/E^2)}{d(1/E)} = -2.84 \times 10^9 \, \Phi^{1.5} \qquad \text{(eq. 8)}$$

intercept:

$$\left[\log\frac{i_{0F}}{E^2}\right] = \log 1.54 \times 10^{-6} \, A_e . \frac{10^{4.52 \, \Phi^{-1/2}}}{\Phi} \qquad \text{(eq. 9)}$$

Describing Fowler-Nordheim equation in a simpler form, we have,

$$J_{0F} = C_1 E^2 \exp(-\frac{C_2}{E}) \qquad \text{(eq. 10)}$$

Where

$$C_1 = 1.54 \times 10^{-6} \times 10^{4.52 \, \Phi^{-1/2}} / \Phi \qquad \text{(eq. 11)}$$

$$C_2 = 6.53 \times 10^9 \, \Phi^{1.5} \qquad \text{(eq. 12)}$$

It should be noted that many authors use the approximation of t(y)=v(y)=1 in the Fowler Nordheim equation. Using the micro protrusions model, we introduce the enhancement factor β into the F-N equation and rewrite it as the following:

$$J_{0F} = C_1 \beta^2 E^2 \exp(-\frac{C_2}{\beta E}) \qquad \text{(eq. 13)}$$

2.2   FIELD EMISSION INITIATING MECHANISMS

Although the fundamental concept of field emission is described by Fowler-Nordheim, the physical procedure and mechanisms through which the electrons discharge from the surface are still being studied today. Different models have been proposed by researchers to describe the mechanisms of field emission among which the micro-protrusion model, the metal-insulator-vacuum model and the metal-insulator-metal model are the most popular. A common feature incorporated into each of these models is

electron discharge from a sharp tip that suffers from contamination (of any kind).

2.2.1 Electron emission based mechanisms

The electric field is enhanced at the tip of the emitter, as shown in Fig. 2.2.1 The localized field is larger than the surface field by a factor β, termed the enhancement factor. Therefore β is the ratio of the higher "microscopic" field at the tip of the emitter to the "macroscopic" surface field at the base of the protrusion.

$$E_m = \beta E \qquad \text{(eq. 14)}$$
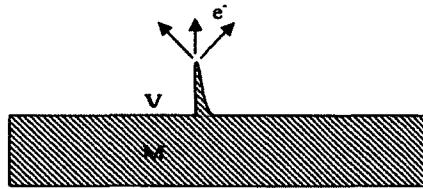
Fig. 2.2.1. Typical field emitter

The enhancement factor β can range from 10 to 1000 based on the geometrical properties of the surface and the shape of the protrusions. Fig. 2.2.2 shows representations of various field enhancement factors associated with different idealized micro-protrusion geometries. Various calculations are done for semi-ellipsoidal or hemispherical or cylindrical projection of the emitters [50, 51]. However the general approximation for β is given as a function of h/r [52],

$$\beta \approx 2 + {}^h\!/_r \qquad \text{(eq. 15)}$$

β

10⁴

Sphere

E = βE₀

r

h

10³

r   E = βE₀

h

Cylinder

E = βE₀

p

h

b

10²

50

Ellipsoid

20

10

2r

6

2r

h

anode

E   d   d≫h

cathode

4

2

1

1   2 4 5 10   10²   10³   10⁴ h/r

1   2   5   10   20   50   100 h/b=λ
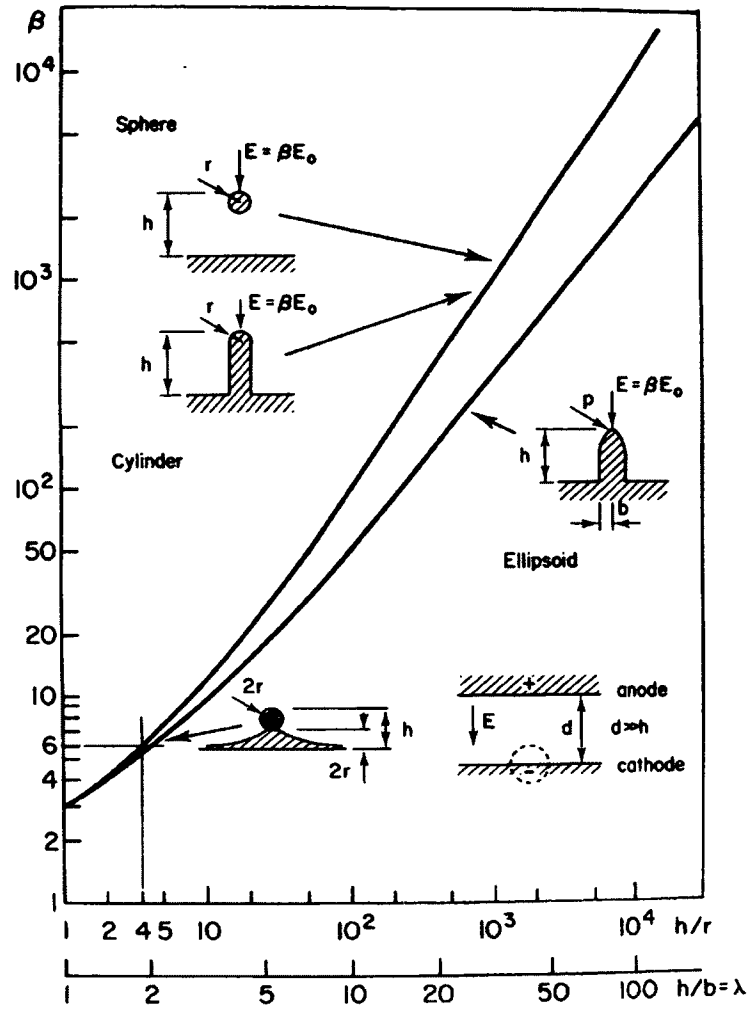
Fig. 2.2.2. Representation of various field enhancement factors beta associated with different idealized micro-protrusion geometries.

β	Spheroid		Cylinder
	h/r	*h/R*	*h/r*
10	9	3	8
100	256	16	98
1000	3600	60	998

Table 2.2.1. β for different geometries.
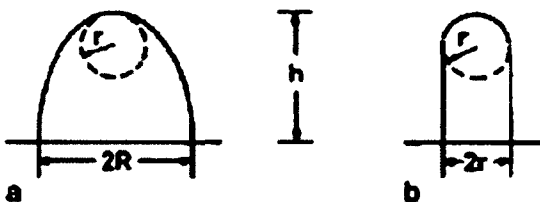
Fig. 2.2.3. Spheroid and cylindrical tip emitters.

2.2.2 Micro-Particle base emission

One of the unavoidable results of the electrode preparation is leaving embedded or loosely attached micro-particles on the surface of electrodes. These particles can be introduced during different stages of preparation. For example, remnants of polishing material like alumina or diamond can be embedded into the cathode surface, or dust-type particles can be attached to the surface of the cathode by Van Der Waals forces during photogun construction. It should be noted that only a specific number of these potential emission sites will be active during high voltage processing because the surface of the electrode is curved and the higher field will occur only at specific regions of the surface

and not equally everywhere.

The very first hypothesis of the micro-particle based mechanisms to initiate the breakdown was given by Cranberg [53]. In his hypothesis he pointed to the process of these micro-particle detachment form the surface by presence of some electro-mechanical forces. After detachment, these liberated particles will be accelerated in the field toward the other electrode and can dissipate their kinetic energy either as heat or some mechanical work on the electrode. If their impact energy exceeds some critical value, they can create a plasma that can make the gap insulation break down. The following are steps of obtaining the critical range required for gap breakdown:

The kinetic energy of the particle is defined as

$$U_k = \frac{1}{2} M_p v_i^2 = Q_p V \qquad \text{(eq. 16)}$$

where M_p is mass of the particle, Q_p is the particle charge and, v_i is the terminal velocity and V is the applied voltage. We know that the charge density is proportional to the macroscopic field E, therefore:

$$\frac{U_k}{A} \propto EV = C'EV \qquad \text{(eq. 17)}$$

where C' is constant. For a critical impact where the conditions in the gap approached the breakdown situation, we will have:

$$\frac{U_k}{A} \geq C'E_b V_b \geq C'd\, E_b^2 \geq C'\frac{V_b^2}{d} \qquad \text{(eq. 18)}$$

where d is the cathode-anode gap.

2.2.3 Detachment criteria

In order to find the particle detachment criteria, we need to equate the charge density localized at the micro-feature which is much higher than the charge density at the surface to the electromechanical forces. However, both of these factors are proportional

to the microscopic electric field at the tip of the emitter and therefore are dependent on the shape of these features. Fig. 2.2.5 illustrates different shapes of idealized micro-features.
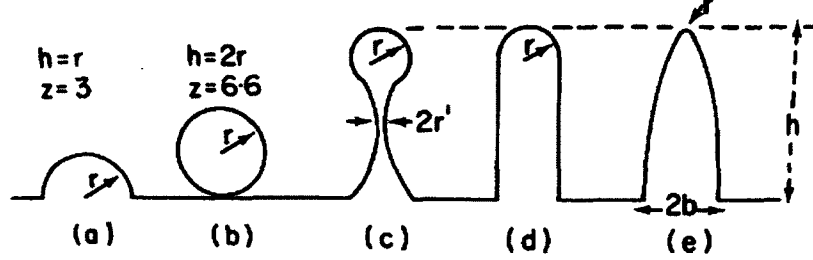
Fig. 2.2.5. Idealized micro-particle structures as potential micro-particle structures [54].

For a spherically based micro-features, where h/r >5, we can define the acquiring charge by the particle as the following,

$$Q_p = 4\pi\varepsilon_0 h^2 \frac{(\beta-3)}{(\beta-2)^2} \cdot E$$ (eq. 19)

For spherical cases a and b in Fig. 4, the charge density is

$$Q_p = z\pi\varepsilon_0 r^2 E$$ (eq. 20)

where z is a numerical factor that should be calculated for specific values of h/r [55,56]. For semi-ellipsoidal micro-feature (Fig. 5e) where $\lambda = h/b$,

$$Q_p(\lambda) = \frac{\pi\varepsilon_0 h^2 \beta}{\lambda^2} \cdot E$$ (eq. 21)

The electromechanical detachment force F_d for spherically based geometries

$$f_d = \frac{4\pi\varepsilon_0(\frac{h}{r}-1)}{(\frac{h}{r})^2} \cdot E^2$$ (eq. 22)

and for semi-ellipsoidal geometry is:

$$F_d(\lambda) = \frac{\pi \varepsilon_0 h^2 f(\lambda)}{\lambda^2} \cdot E^2 \qquad \qquad \text{(eq. 23)}$$

where $\quad \lambda = h/b \quad$ and $\quad f(\lambda) = \frac{\beta^2(\lambda)}{2(\lambda^2-1)} \left[\frac{\lambda^2}{\lambda^2-1} log\lambda^2 - 1\right] \qquad$ (eq. 24)

we can obtain the detachment conditions when the electromechanical forces be equal to the yield stress of the electrode material. Therefore this condition for the spherical and semi-ellipsoidal geometry are as the following respectively.

$$\frac{F_d}{\pi r^2} \geq \sigma_y \quad \text{therefore} \quad 4\pi\varepsilon_0 \left(\frac{h}{r} - 1\right) E^2 \geq \sigma_y \qquad \text{(eq. 25)}$$

$$\frac{F_d(\lambda)}{\pi b^2} \geq \sigma_y \quad \text{therefore} \quad \varepsilon_0 f(\lambda) E^2 \geq \sigma_y \qquad \text{(eq. 26)}$$

CHAPTER 3

EXPERIMENT DESCRIPTION

Pierce-type cathode electrodes with 25 degree focusing angle (6.35 cm dia., 2.85 cm thick) were attached to an inverted insulator that extends into the ultrahigh vacuum test chamber (Fig. 3.1). Each electrode had a shape identical to electrodes used at the Continuous Electron Beam Accelerator Facility (CEBAF) for many years [57] with a hole in the middle (1.28 cm dia.) to accommodate a GaAs photocathode if it were used in an actual polarized photogun. However for these tests, a piece of polished stainless steel was used in place of the GaAs photocathode.

The anode was a flat plate with a Rogowski edge profile, electrically isolated from ground and attached to a sensitive current meter (Keithley electrometer model 617). The anode could be moved up or down to vary the cathode/anode gap and therefore the field strength. Two different anodes were used for these tests: a 304 stainless steel anode for evaluation of stainless steel cathode electrodes and a fine-grain niobium anode for evaluation of all the niobium cathode electrodes. The stainless steel anode was polished with 600 grit silicon carbide paper and 6 μm diamond paste. The fine-grain niobium anode was chemically polished.

Insulator

Test Electrode
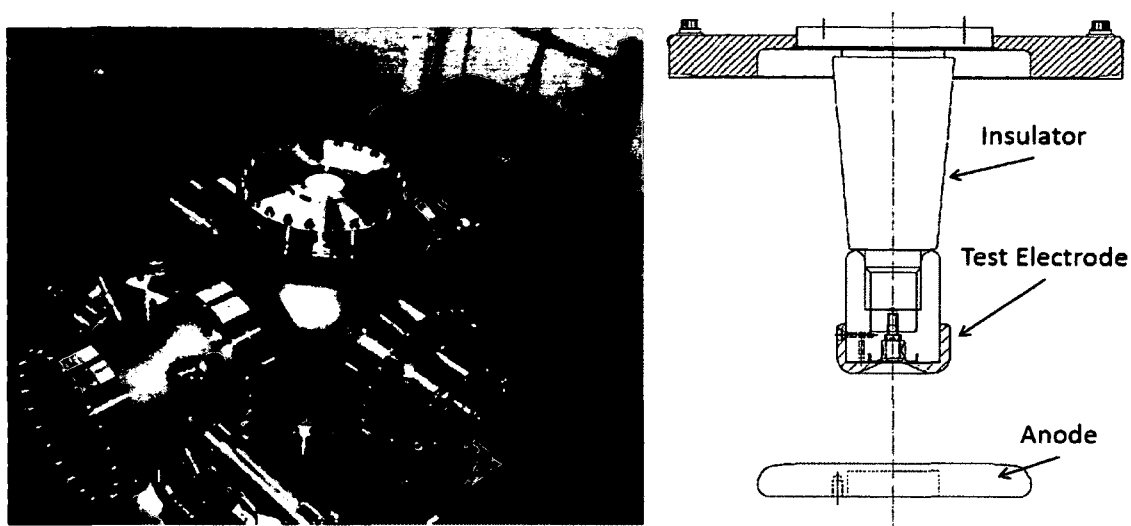
Anode

Fig. 3.1.1. (left) Photograph of the dc high voltage field emission test stand used to evaluate each cathode electrode, (right) a schematic view of the insulator, test electrode and anode used to collect the field emission.

A -225 kV commercial high voltage power supply was used for the experiment. The HV power supply and the ceramic insulator accommodate "industry standard" high voltage cables with R-28 connectors. A 100 M□ conditioning resistor was placed in series with the cathode electrode via an oil tank and served to protect the apparatus in case of sudden discharge of stored energy. The resistor also serves to protect the electrode via a negative feedback mechanism – as current increases, a larger voltage drop occurs across the resistor, reducing voltage at the electrode.

Each test electrode underwent similar preparation steps before installation as described below. Prior to the application of high voltage, the entire vacuum apparatus was baked at 200°C for 30 hours to achieve vacuum level in the -11 Torr range. Vacuum pumping was provided by a 220 L/s ion pump and a SAES Getters GP-500 non-evaporable getter pump which was partially activated during the bakeout. Every effort was made to keep the vacuum conditions constant from sample-to-sample, but depending on the amount of water vapour that was introduced into the apparatus upon venting and

replacing the electrode, the vacuum could vary by factors of two or three between tests.

An assessment of the field emission properties of each test electrode involved monitoring vacuum level inside the apparatus, x-ray radiation near the apparatus, and anode current while increasing the voltage applied to the cathode electrode. High voltage was first applied to the electrode using the largest cathode/anode gap of 50 mm. Upon successful high voltage processing (defined below), the gap could be decreased to achieve higher field strength. The smallest gap was 20 mm and provided maximum field strength of ~ 20 MV/m when the cathode was biased at -225 kV. Gap spacing less than 20 mm was avoided, as small gaps sometimes produced catastrophic breakdown and electrode damage.

Voltage was applied to each electrode and increased gradually while maintaining anode current less than a few nanoAmperes. During processing, field emission sites would "burn off" and field emission current would become more stable. An electrode was considered fully processed when field emission current was stable to within a few percent of the average value. It was not uncommon for this to take many hours.

High voltage processing was not always successful: sometimes a field emission site (or sites) would be produced that would not burn off. This typically happened at the smallest gaps and highest field strengths. Elimination of stubborn field emitters often required krypton-processing (described below), or worst case, the electrode was removed and re-polished.

Diamond Paste Polishing of Stainless Steel

The field emission characteristics of niobium electrodes were benchmarked against those of conventional DPP stainless steel electrodes that had been used successfully for many years inside one of the CEBAF 100kV spin polarized photoelectron guns. The DDP stainless steel electrodes were manufactured from vacuum arc-remelt 304 stainless steel. After being cut to shape with hydrocarbon-free lubricants, each electrode was polished on a potter's wheel with silicon carbide paper of increasingly finer grit (300 and then 600 particles/in^2) followed by polishing with diamond grit (6 μm, 3 μm). This produced an electrode with a mirror-like finish. Between each polishing step, the electrode was cleaned in an ultrasonic bath using an alkali solution. The steps for

preparing a DPP electrode were as follows:

- Receive the electrode from the machine shop with "32" surface finish [58]
- Silicon carbide polishing with 300 grit paper to remove obvious visible scratches
- Solvent cleaning in ultrasonic bath of alkali solution
- Silicon carbide polishing with 600 grit paper
- Solvent cleaning in ultrasonic bath of alkali solution
- Polish with 6µm grit
- Ultrasonic clean
- Polish with 3□m grit
- Ultrasonic clean
- High pressure rinsing (1200 psi) for 20 minutes with ultrapure de-ionized water with resistivity > 18 M□cm.
- High temperature (900°C) vacuum degas for one hour

Buffered Chemical Polishing of Niobium

Three different types of niobium electrodes were evaluated: single-crystal, large-grain (grain size > few cm) and fine-grain (also referred to as poly-crystalline, grain size ~ 0.13 mm). The single-crystal and large-grain niobium test electrodes were manufactured from high quality material suitable for SRF cavity fabrication with residual resistance ratio (RRR) values > 250. The fine-grain niobium electrode was manufactured from "reactor grade" material with RRR value ~ 40. Machined electrodes were chemically etched in a mixture of hydrofluoric (49%), nitric (69%) and phosphoric (85%) acid with mixing ratio 1:1:1 at room temperature. This technique is referred to as buffered-chemical polishing. Typically, the desired surface finish was obtained after ~ 20 minutes immersion in the acid bath, corresponding to removal of 100 µm of surface material. Besides taking advantage of the SRF technique of buffered-chemical polishing, other SRF techniques were adopted including high pressure rinsing and vacuum degassing [58]. The steps for preparing a polished niobium electrode were as follows:

- Receive the electrode from the machine shop with "32" surface finish [59]
- Silicon carbide polishing with 600 grit paper, if necessary, to remove obvious visible scratches

- Solvent cleaning in ultrasonic bath of alkali solution

- Buffered-chemical polishing to remove ~ 100 μm material

- High pressure rinsing (1200 psi) for 20 minutes with ultrapure de-ionized water with resistivity > 18 MΩcm.

- High temperature (900°C) vacuum degas for one hour

Electropolishing of stainless steel

Electropolishing is a widely used technique to smooth metallic surfaces, for example to reduce the surface area of vacuum chambers and thereby reduce the gas load due to hydrogen outgassing [60]. A number of photogun groups have tested electropolished electrodes inside DC high voltage photoguns, however field emission remains a significant problem preventing operation at 500 kV [61, 62].

During electropolishing, the piece to be polished is immersed in an electrolytic bath, typically acid, and biased positive. A nearby sacrificial electrode is biased negative and current passes between the two electrodes. The surface of the piece being polished becomes oxidized and this oxide layer dissolves away. For the process to be successful, the protrusions at the surface must dissolve faster than the recesses. A number of important parameters can influence the efficacy of electropolishing, including the temperature of the electrolytic bath, the types and concentration of acids used, and the rate at which the solution passes across the work piece surface. For this work, the electrodes were electropolished by a commercial vendor [63], using a proprietary process, but one considered to be relatively generic in terms of the technique. Electropolishing resulted in the removal of approximately 10 μm of material from the surface.

3.1 ESTIMATING THE FIELD STRENGTH USING POISSON

The electrostatic field mapping program POISSON [64] was used to estimate the field strength between cathode and anode, as a function of the applied cathode voltage

and the cathode/anode gap. The highest surface field was located along an annular region with radius slightly larger than the portion of the electrode closest to the anode (Fig. 3.1).
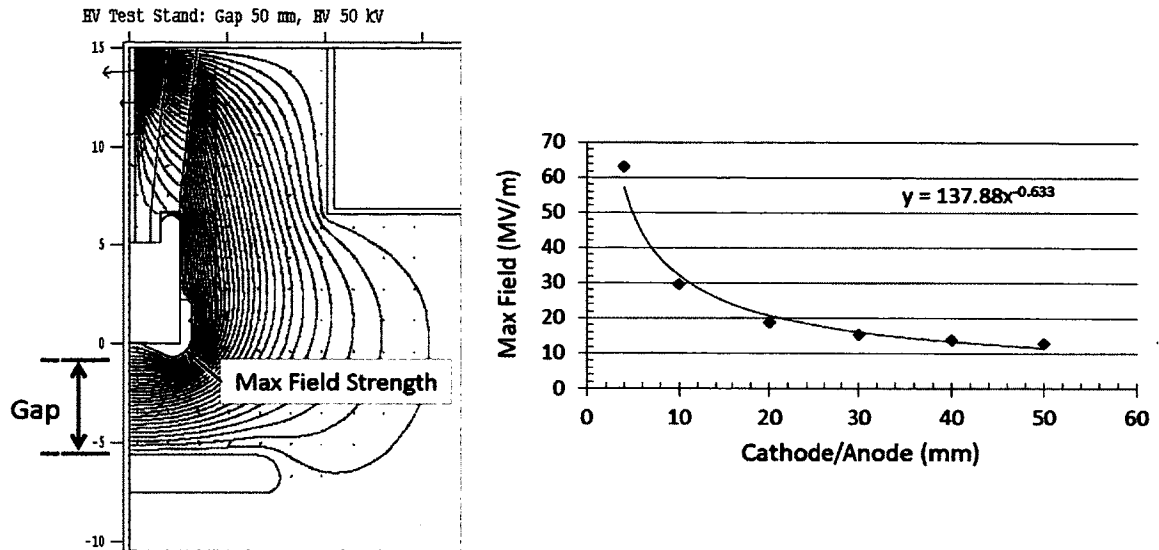
Fig. 3.1.2. (left) POISSON electrostatic field map showing lines of constant potential inside the field emission test apparatus. (right) Maximum field strength as a function of anode/cathode gap for 225 kV cathode bias voltage. Data points are from POISSON and the line is a simple fit using a power function

3.2 ELECTRODE CONDITIONING

3.2.1 Current Conditioning

Current conditioning is typically the default technique for "processing" a new (virgin) electrode, whereby voltage is applied to the electrode in small increments, allowing the pre-breakdown field emission current to stabilize and frequently, the field emission current decreases to a smaller level over time as field emission sources "burn off". This sequence is shown in Fig. 3.2.1. This figure also shows the sudden fall in pre-breakdown current that is indicative of a field emitter burn off.
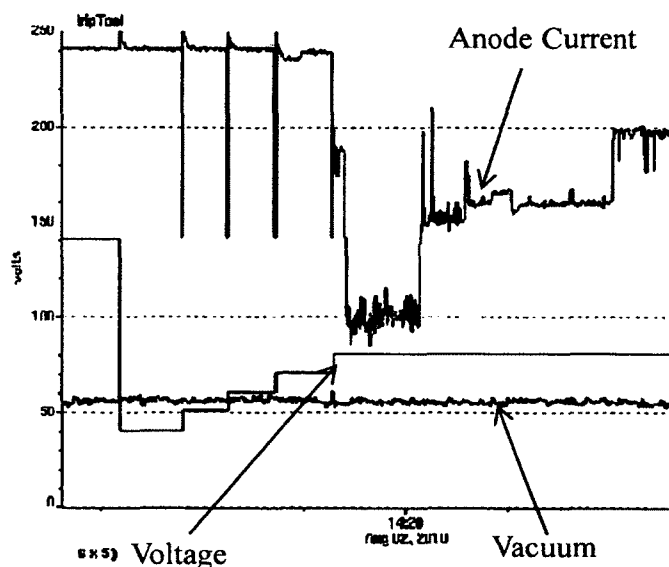
Fig. 3.2.1. Anode Current, voltage and vacuum signals during current conditioning.

3.2.2 Gas Conditioning

Gas conditioning as a means to reduce field emission current was originally introduced by Lyman et al., in 1966 [65-67] and later used by Bekuma [67, 68]. Alpert et al. [58], showed that gas ions selectively bombard metallic micro-protrusions at a higher rate, based on the site's localized field enhancement factor, β. For a time, the effectiveness of gas conditioning was assumed to be related to the transformation of sharp tips into blunt tips, by the process of sputtering. But when gas conditioning was also demonstrated to eliminate field emission from non-metallic emitters [69-71], a full appreciation of the technique grew to include ion implantation which serves to increase the work function of the metal. Latham termed "current quenching" for ion implantation and associated field emission reduction, and presented experimental evidence that current quenching was electronic in origin [72, 73]. He studied a variety of gasses (H_2, D_2, He, Ar, N_2, SF_6) and demonstrated that each was effective at eliminating field emission but the voltage at which the process was performed was a critical parameter, indicating that helium was more effective at eliminating field emission at lower voltage while heavier gasses were more effective at higher voltage [74].

The electron impact ionization probabilities (cross section) for helium and krypton

are plotted in Fig.3.2.2a as a function of electron beam energy [75, 76]. The two curves mimic each other, however with the ionization probability of krypton roughly an order of magnitude higher than helium. The peak ionization for both gas species occurs at ~ 100V, and dropping by more than three orders of magnitude at 225kV, which is the maximum voltage studied in this work. It is important to note that the energy spectrum of the field emitted electrons within the cathode/anode gap is broad, with electrons leaving the cathode electrode at zero velocity, and then gaining energy until reaching the anode. Ionization probabilities were used to estimate the total ion yield as a function of location within the cathode/anode gap at 200kV in Fig.3.2.2b, with a gas pressure 5e-6 Torr and 13nA of field emission current corresponding to 200kV, and for a cathode/anode gap of 3 cm. Nearly half of all ions originate within 1 mm of the cathode electrode surface.

From a sputtering point of view, massive krypton will be more effective at turning sharp field emitter tips into blunt tips compared to helium, but other factors must be considered when implementing gas conditioning inside a DC high voltage photogun, including the cathode/anode geometry, the orientation of electrostatic field lines, and where the ions are created within the cathode/anode gap. Most DC high voltage photoguns employ curved electrodes, which in turn, produce curved electric field lines. Electrons will follow these curved electric field lines but comparatively slow moving ions will have trajectories that can deviate significantly. Only ions produced at locations with straight electric field lines, or near the cathode surface are guaranteed to impact the electrode near the field emitter.

In summary, the location where the ion was created within the cathode/anode gap determines the energy of the ion at impact, which in turn influences sputtering yield and implantation depth. The curved field lines will reduce the likelihood of higher-energy ions produced near the anode reaching the field emitter.
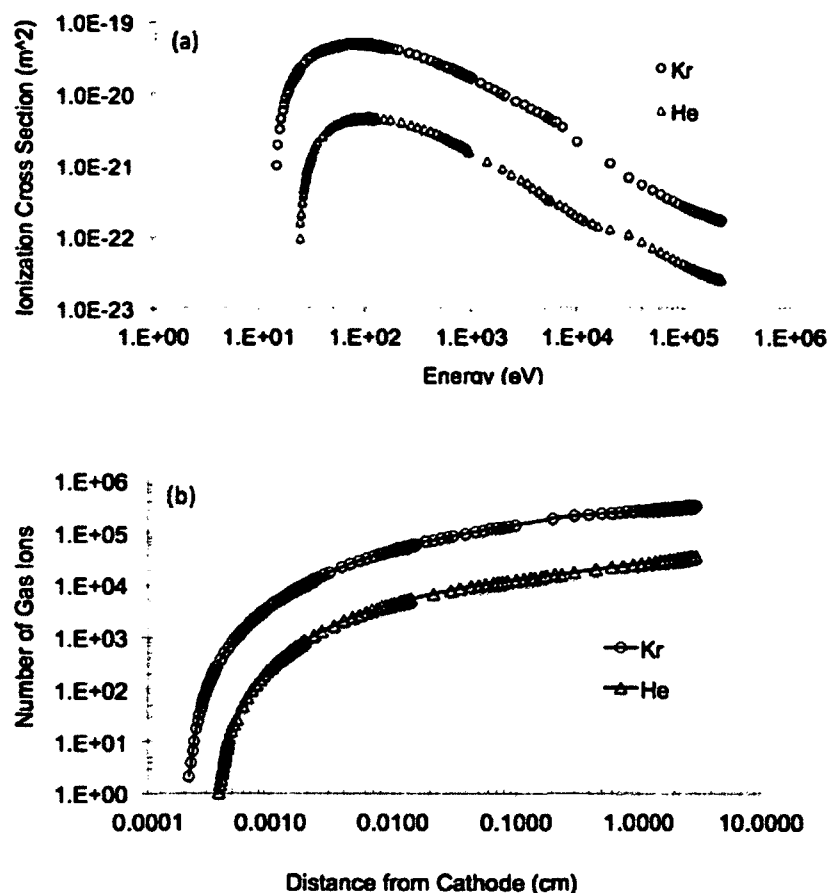
Fig. 3.2.2.a. Ionization cross section for helium and krypton, b. Calculated ion yield as a function of distance from the cathode surface assuming pressure 5e-6 Torr and field emission current of 13 nA at 200kV.

Gas Conditioning Protocol

Gas conditioning involved introducing an inert gas into the vacuum chamber while the cathode electrode was biased at high voltage using a gap/field strength that produced significant field emission (~ few □As or lower). Gas was introduced to the vacuum apparatus via a leak valve set to provide pressure in the range of ~ 5e-6 to ~5e-4 Torr [77]. A sudden reduction in anode current was indicative of the elimination of a field emission site. Gas conditioning typically was performed for 30 to 60 minutes and

repeated multiple times, depending on the performance of the test electrode in the field emission reduction process.

Considerable care was taken to ensure the recovery of good vacuum post-gas conditioning. The procedure involved continuously pumping the supplied gas using a turbo pump appended to the apparatus behind a baked right angle valve. During gas processing, the ion pump was turned off to avoid overburdening the pump with gas not efficiently pumped. When the gas processing was completed, the gas supply was terminated and the turbo pump was allowed to pump on the apparatus for an additional ~ 15 minutes. The ion pump was then re-energized and the valve to the turbo pump closed. Vacuum within the apparatus recovered relatively quickly (~ 24 hours) because care was taken to avoid back-streaming water vapor into the apparatus. Additionally the non-evaporable getter pumps maintained high pump speed since they do not pump inert gasses.

Inert gas pressure and cathode/anode gap could be varied to observe two distinct anode current trends: current amplification and current quenching. Current amplification can be explained by noting that the ionization of the supplied gas produces additional free electrons that travel to the anode in addition to those originating from field emission sites. Furthermore, ions bombarding the cathode electrode, and electrons striking the anode electrode desorb additional gas (most likely surface-bound hydrogen) that can in turn become ionized. The other trend – current quenching – describes the situation where the observed anode current is reduced during gas conditioning. This phenomenon occurs when a sufficient number of ions blanket the electrode surface, increasing the work function of the material, thereby quenching the field emission (at least temporarily, during gas conditioning).

Fig. 3.2. shows examples of both anode-current trends observed using the same electrode but under different conditions: helium pressure 5e-5 Torr versus 5e-6 Torr, and cathode anode gap 10 and 30 mm. The black (blue) lines represent the observed anode current before (during) gas conditioning, as a function of applied high voltage. It was not obvious that one condition was more effective at reducing field emission than the other.
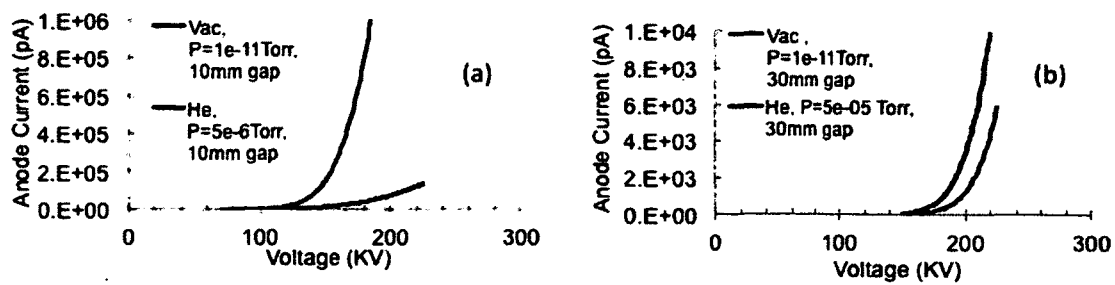
Fig. 3.2.3.　Examples of (a) anode current quenching, and (b) anode current amplification, during helium gas conditioning at different pressures and gaps

CHAPTER 4

REDUCTION OF FIELD EMISSION FROM STAINLESS STEEL ELECTRODES

USING GAS CONDITIONING WITH HELIUM AND KRYPTON

Five stainless steel electrodes (304L and 316LN) were polished to approximately 20 nm surface roughness using diamond grit and evaluated inside an ultrahigh vacuum test stand to determine the onset of field emission as a function of voltage and field strength. The field emission characteristics of each electrode varied significantly upon the initial application of voltage. The performance of all electrodes improved to nearly the same level after helium and krypton gas conditioning, exhibiting field emission less than 10 pA at - 225kV bias voltage and for a 50 mm cathode/anode gap, corresponding to a field strength ~ 13 MV/m. Field emission could be reduced with either gas, but there were conditions related to gas choice, voltage and field strength that were more favorable than others. Measurements and simulation using the computer programs SRIM/TRIM suggest that gas conditioning effectively eliminates field emission sites via sputtering but also as a result of ion implantation which could serve to increase the work function at the surface of the electrode. Heating the cathode was found to partially reverse the benefits of ion implantation, which we speculate serves to deplete the electrode surface of implanted ions by desorption and diffusion.

4.1   RESULTS: FIELD EMISSION VERSUS VOLTAGE

The field emission characteristics of four diamond-paste polished stainless steel electrodes are presented in Fig. 4.1 Each plot shows field emission current as a function of voltage at four different cathode-anode gaps, before and after gas conditioning. During the initial application of voltage, the 304L electrodes exhibited field emission at bias voltage at or below 100kV, whereas the 316LN electrode performed better, with field emission onset ~ 150kV or higher. It should be noted that the small sample set precludes making a definitive statement about properties of specific grades of steel.

After gas conditioning, all four electrodes exhibited similar performance, with no field emission (< 10pA) at 50mm gap and 225kV bias voltage. Gas conditioning was performed with both helium and krypton gasses to determine which was more effective. After field emission characterization, the surface of each electrode was scanned using an optical profilometer to determine roughness. As mentioned above, the surface roughness of the electrode samples varied from 10 to 30 nm but no correlation between field emission performance and roughness was found.
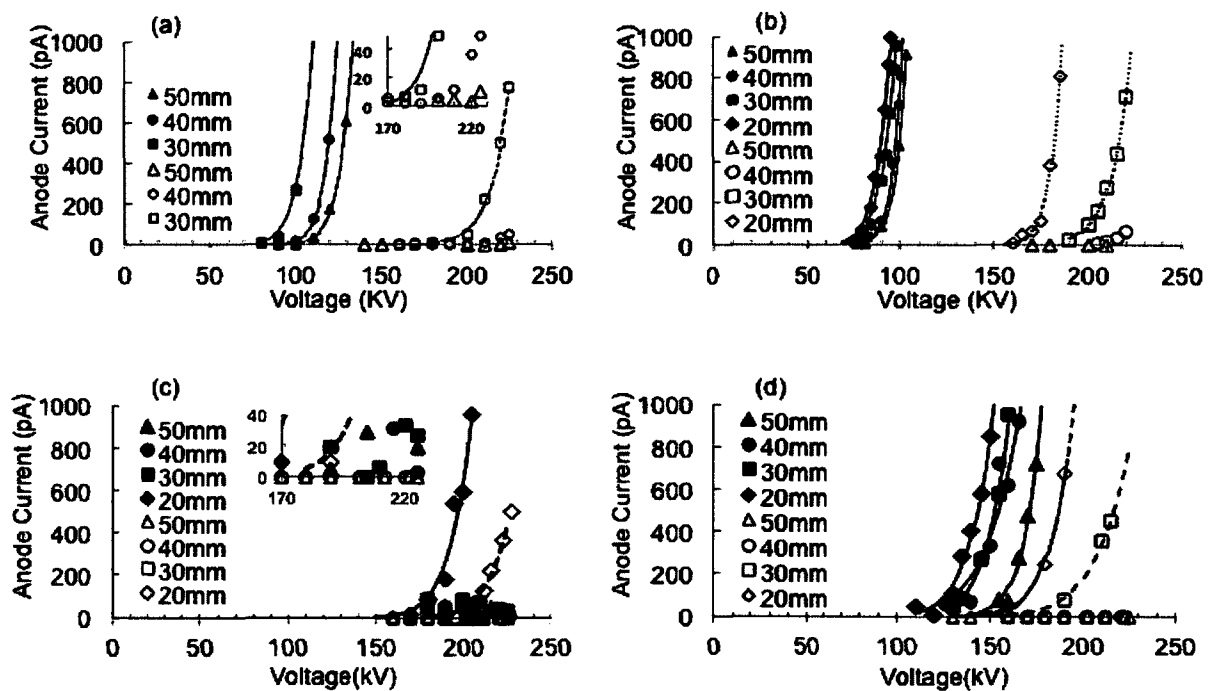
Fig.4.1. Field emission current versus bias voltage and anode/cathode gap for 304L stainless steel electrodes (top) and 316LN electrodes (bottom). Each plot shows field emission behavior before (solid symbols) and after (open symbols) gas conditioning with helium and krypton. For all cases the lines between data points represent Fowler-Nordheim fits.

The electrostatic field mapping program POISSON [64] was used to estimate the field strength between the cathode and anode, as a function of the applied cathode voltage and cathode/anode gap. The highest field was located along an annular region with radius slightly larger than the portion of the electrode closest to the anode. Table 4.1 lists the

field strength at which each electrode (using the results of Fig. 4.1) produced 100 pA of field emission. The value 100 pA was chosen because it was large enough to accurately apply a Fowler-Nordheim fit to the data. Before gas conditioning most of the electrodes exhibited field emission at field strengths between 5-10 MV/m. After gas conditioning, for the gaps 40 and 50 mm, none of the electrodes exhibited 100pA of field emission corresponding to field strengths 13.8 and 12.6 MV/m, respectively.

Turn on Field Strength at 100pA , Before Gas Processing vs. Gaps

Gap(mm)	304L#1	304L#2	316LN#1	316LN#2
50	6.4	4.9	>12.6	8.7
40	6.6	5.4	>13.8	8.1
30	6.2	5.5	>15	9.1
20		6.6	15	10.5

Turn on Field Strength at 100pA , After Gas Processing vs. Gaps

Gap(mm)	304L#1	304L#2	316LN#1	316LN#2
50	>12.6	>12.6	>12.6	>12.6
40	>13.8	>13.8	>13.8	>13.8
30	13.6	13.5	>15	12.9
20		14.4	17.3	14.1

Table 4.1. The field strength at which each electrode exhibited 100 pA of field emission at different gaps before and after gas conditioning. For entries with (>) symbol, field emission current did not exceed 100 pA at -225 kV, and consequently, the field strength must exceed the maximum value provided by the high voltage power supply.

4.2 FOWLER –NORDHEIM "LINE PLOT" ANALYSIS

It is common to replot I-V curves like those shown in Fig. 4.1 as Fowler-Nordheim logarithmic line plots, which can be used to estimate the field enhancement factor, β□□ and the field emission emitter area, A_e , using the expressions below that originate from Eq.1.

$$slope = \frac{d(log_{10}I/E^2)}{d(1/E)} = -\frac{2.84 \times 10^9 \varphi^{1.5}}{\beta} \qquad \text{eq. 4}$$

$$intercept = Log_{10}(I_F/E^2)_{E \to \infty} = Log_{10}[\frac{1.54 \times 10^{-6} A_e \beta^2 \times 10^{4.52\varphi^{-0.5}}}{\varphi}] \qquad \text{eq. 5}$$

These expressions assume a single field emitter tip, which is not realistic for large-area electrodes, however the exercise can still provide insight, as will be demonstrated below. Fig. 4.2 shows a Fowler-Nordheim line plot analysis of one of the 304L stainless steel electrodes at three different cathode/anode gaps, before and after gas conditioning with helium. Gas conditioning resulted in a significant reduction in the calculated field enhancement factor, □, from 972 to 299. And the calculated emitting area increased from 8.4e-20 to 7.1e-17 m^2, consistent with the notion that field emitter tips become blunted and wider as a result of gas conditioning. Similar results were observed for the other electrodes as listed in Table 4.2.
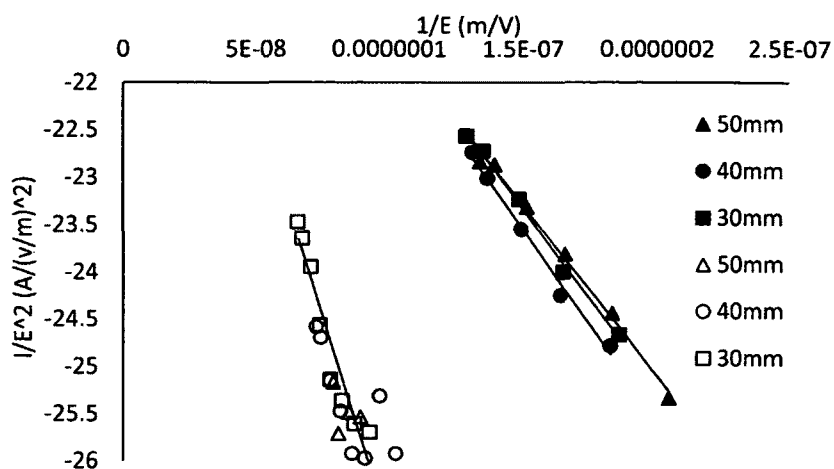
Fig. 4.2. Folwer-Nordheim line plot analysis for a 304L stainless steel electrode, before (solid symbols) and after (open symbols) gas conditioning with helium.

	304L#1	304L#2	316LN#1	316LN#2
Beta/pre Gas	228	972	217	475
Beta/Post Gas	134	299	185	171
A_e/ pre gas	9.7E-19	8.4E-20	1.7e-17	2.5E-20
A_e/ post gas	1.1E-17	7.1E-17	3e-17	3.1E-10

Table 4.2. Summary of Fowler-Nordheim line plot analysis: field enhancement factor, β, and emitting area, A_e , before and after gas conditioning, for four stainless steel electrodes.

4.3 HELIUM VERSUS KRYPTON

Effort was devoted to determining the relative effectiveness of helium versus krypton. Electrodes were conditioned with one gas under different pressure and gap

conditions, and then conditioned using the other gas. However, the performance of the electrode was very difficult to control: once the electrode performance improved to a high level, further gas conditioning was not possible (i.e., the electrode did not field emit and consequently, ions were not created). Smaller gaps could be used to achieve significantly higher field strength, which could initiate more field emission, but often small gaps resulted in breakdown which damaged the electrode. Fig. 4.3 shows representative results using different gas species, pressure and gap conditions for two electrodes. These and similar results from other electrodes, led to the following generalized observation: helium was more effective at eliminating field emission using lower voltage and smaller gaps, whereas krypton was more effective at higher voltage and larger gaps. But it must be stated that this is a very preliminary "conclusion": there were examples of effective field emission reduction under conditions contrary to this statement that could be related to effects of any gas on a virgin electrode regardless of the gas kind. It must also be noted that krypton gas conditioning at small gaps sometimes resulted in degraded performance, serving to enhance field emission.
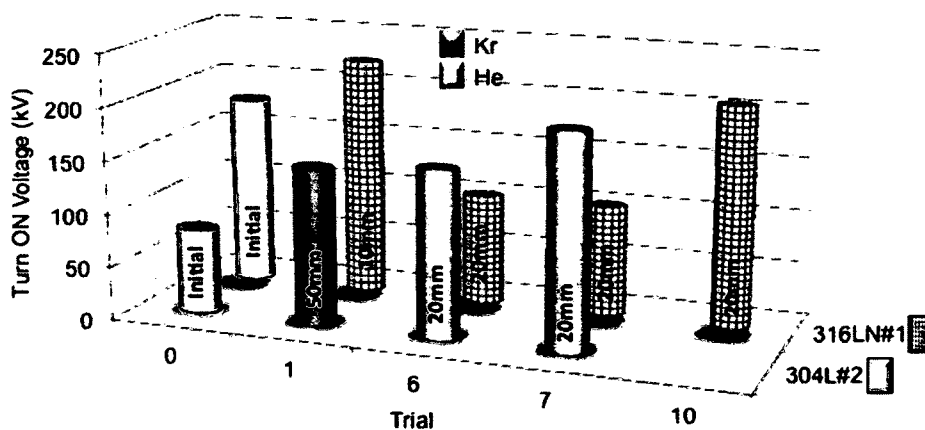
Fig. 4.3. The voltage that could be reached without field emission (< 10pA) at 30 mm gap, as a function of gas conditioning trial. Annotations denote the gas species, gap and pressure conditions for each trial.

4.4   TRIM/SRIM ANALYSIS

To better understand the experimental results, the computer simulation codes SRIM and TRIM (Stopping Range of Ions in Matter, and Transport of Ions in Matter) [78] were used to estimate the stopping depth of implanted gas ions within the cathode electrode and the level of sputtering. Fig. 4.4.1 shows the number of implanted ions and the stopping depth for helium (left) and krypton (right), as a function of ion energy. These plots were obtained at field emission of 150 pA, a cathode/anode gap of 30 mm, and pressure 5e-6 Torr. The number of ions for each energy was scaled using the ionization probability curves shown in Fig. 4.1.

Comparing the two simulations, it is obvious that helium ions penetrate much deeper into the stainless steel compared to krypton: helium ions are implanted at depths ranging from 1000 to 7000 nm, whereas krypton ions at implanted at depths < 1000 nm. Assuming implanted ions serve to reduce field emission (at least in part) due to increased work function, it would be beneficial to helium gas process at lower voltage, where the implanted ions are closer to the surface. This result is consistent with experimental observation – helium gas processing was generally more effective at lower voltages and smaller cathode/anode gaps. More massive krypton ions are implanted at shallow depths for all ion energies tested. Consequently, krypton ion implantation would serve to increase the work function of the electrode for any ion energy tested.

32

(a)

Number of Ions

5.E+05
4.E+05
3.E+05
2.E+05
1.E+05
0.E+00

100 1100 2100 3100 4100 5100 6100 7100

70 keV
130 keV
190 keV
225 keV

Implantation Depth (A)

(b)

Number of Ions

5.E+05
4.E+05
3.E+05
2.E+05
1.E+05
0.E+00

100 2100 4100 6100 8100 7100

70 keV
130 keV
190 keV
225 keV

Implantation Depth (A)
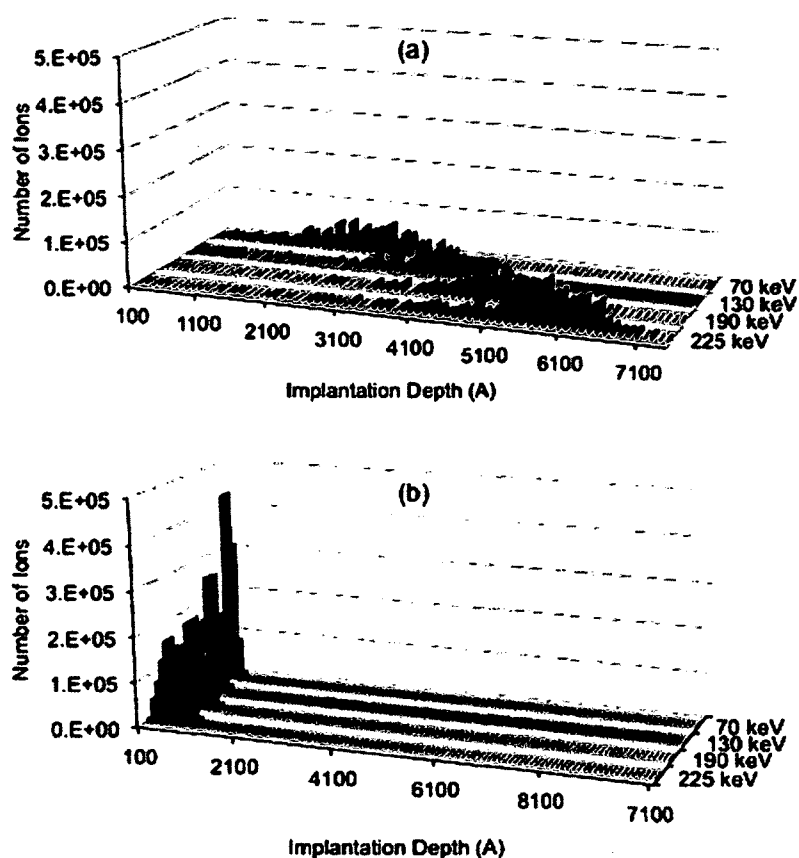
Fig. 4.4.1. Helium (top) and krypton (bottom) ion implantation depth as a function of ion energy. The scales on both plots are identical to provide easy interpretation of the results.

Fig. 4.4.2 shows the results obtained using the program TRIM, which characterizes the sputtering yield of helium and krypton ions on stainless steel, as a function of ion energy. Krypton has a significantly higher sputter yield compared to helium, over the entire ion energy range tested. For krypton ions with energy greater than 1 kV, multiple atoms are sputtered from stainless steel for each bombarding krypton ion, whereas many helium ions are required to sputter away a single atom from stainless steel over the entire energy range tested. This would certainly be beneficial when dealing with an electrode suffering from contamination, and sputtering would serve to transform sharp tips into blunt tips, assuming the ions are delivered to the emitter. But excessive sputtering can

lead to enhanced field emission [79] and this could potentially explain why sometimes krypton gas conditioning resulted in higher levels of field emission from test electrodes.

1.E+01

1.E+00

1.E-01

Sputtering Yield (Atoms/ion)

1.E-02

1.E-03

○ Krypton

△ Helium

1.E-04

0.01   0.10   1.00   10.00   100.00

Energy (keV)
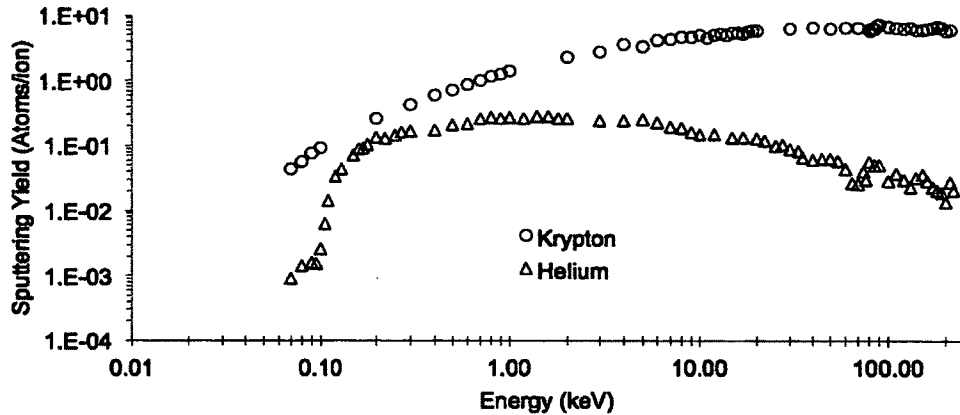
Fig. 4.4.2. Sputtering yield of helium and krypton ions on stainless steel, versus ion energy.

4.5   REVERSING THE EFFECTS OF GAS CONDITIONING

In order to decouple the benefits of ion implantation and sputtering, a fifth stainless steel electrode was gas conditioned and then heated to 250 °C in situ, for approximately 8 hours, using a small heater inserted into the bore of the ceramic insulator. The logic behind the heating test was the following. If the field emission suppression mechanism was purely due to sputtering, then heating would not change the field emission current after conditioning. If the mechanism was purely due to changes in the work function, then heating would reverse the field emission current back to levels prior to conditioning. Fig. 4.5a shows field emission current as a function of voltage for one of the 316LN electrodes at 40 mm gap before (solid black circles) and after (open black circles) gas conditioning, as well as after cathode heating (red). The field emission levels increased after heating, but the electrode still performed better than it did initially, suggesting that the cumulative benefit of gas conditioning is composed of both sputtering and ion implantation, with the latter being reversible. These results indicate that heating the

electrode served to enhance diffusion of ions within the material, and to degas weakly bound gas ions that might have collected at the surface.

The post-krypton conditioning results and the post-heating results shown in Fig. 4.5a were graphed as Fowler-Nordheim line plots (Fig. 4.5b). The post-heating results provide a numerical assessment of the field enhancement factor β. It is reasonable to assume that heating the electrode does not change the physical characteristics of the electrode (i.e., β remains the same). Using the previously calculated value for β, the work function must increase by ~ 1.1eV to fit the post-krypton processing result, an amount consistent with reports in literature [80].
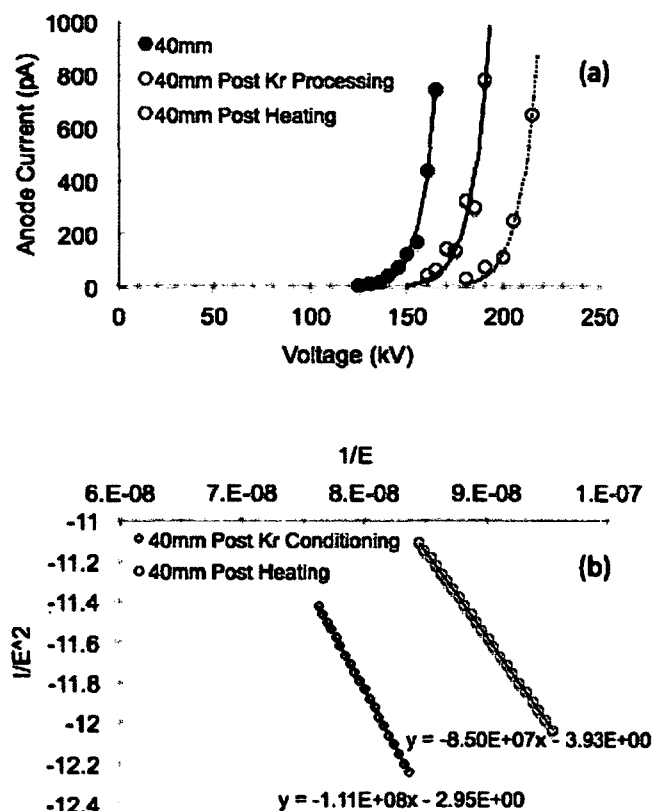
Fig.4.5. a) Field emission current as a function of bias voltage for a 40mm cathode/anode gap, before (black) and after (open) gas conditioning and after heating (red). b) Fowler-Nordheim line plots of the results shown above. The change in slope of the two lines was used to estimate the change in the work function associated with ion implantation.

4.6   CONCLUSION

Five stainless steel electrodes (304L and 316LN) were polished to approximately 20 nm surface roughness using diamond grit and evaluated inside an ultrahigh vacuum test stand to determine the onset of field emission as a function of voltage and field strength. The field emission characteristics of each electrode varied significantly upon the initial application of voltage, with the 316LN stainless steel electrodes performing better than the 304L stainless steel electrodes. The performance of all electrodes improved to nearly the same level using gas conditioning with helium and/or krypton, with field emission less than 10 pA at –225 kV bias voltage and for a 50 mm cathode/anode gap, corresponding to a field strength ~ 13 MV/m. Some electrodes reached higher field strengths without field emission, at smaller gaps. Field emission could be reduced using either gas, but helium gas conditioning was more effective at lower voltage and small gaps (10-20mm), whereas krypton gas conditioning was more effective at higher voltages and larger gaps (30 - 50 mm). Both gasses were effective at pressures in the range of 5 to 50 e-6 Torr and the benefits of gas conditioning were typically realized during ~ 20 minutes-long processing periods.

Measurements and accompanying simulation results obtained using the computer simulation codes SRIM/TRIM suggest that gas conditioning effectively eliminates field emission sites via sputtering but also as a result of ion implantation which serves to increase the work function of the electrode. This statement is supported by the observation that field emission suppression effects of ion implantation could be partially reversed by heating the electrode, which depletes the electrode surface of implanted ions due to desorption and diffusion. The simulation results also support the observation that helium gas conditioning was more effective at lower voltages because this yields a shallow implantation depth, which is better suited to increasing the work function of the metal. Empirical observations reported in Ref. 14 are now understood with the contributions presented in this work.

There are practical considerations associated with gas conditioning that were not addressed experimentally or using the simulation software, namely, curved electrodes

generate curved field lines. For example, krypton offers advantages over helium: it is easier to ionize compared to helium and has a higher sputtering yield, however, depending on location of the field emitter, krypton ions may not follow the field lines to the location of the field emitter. Another issue that was not raised in the paper relates to x-ray radiation – krypton ion bombardment generates significantly higher levels of x-ray radiation which could conceivably be problematic for some users depending on their available shielding.

Future work could employ an ion gun to sputter-clean and implant the entire electrode, rather than just locations near an active field emitter. The ion gun would also provide a monochromatic ion beam that could provide a more accurate experimental assessment of sputter yield and the most effective implant depth, and conditions could be more accurately modeled.

The results and methodologies presented are highly significant to the present development of 500kV DC photoemission guns at various institutions (Cornell, JLab, JAEA) with the goal to generate ultra-bright electron beams required for proposed Free Electron Lasers based on energy recovery accelerators to produce X-ray beams with unprecedented flux and brilliance.

CHAPTER 5

DC FIELD EMISSION EVALUATION OF NIOBIUM AS CANDIDATE ELECTRODE MATERIAL FOR DC HIGH VOLTAGE PHOTOELECTRON GUNS

The field emission characteristics of niobium electrodes were compared to those of stainless steel electrodes using a DC high voltage field emission test apparatus. A total of eight electrodes were evaluated: two 304 stainless steel electrodes polished to mirror-like finish with diamond grit and six niobium electrodes (two single-crystal, two large-grain and two fine-grain) that were chemically polished using a buffered-chemical acid solution. Upon the first application of high voltage, the best large-grain and single-crystal niobium electrodes performed better than the best stainless steel electrodes, exhibiting less field emission at comparable voltage and field strength. In all cases, field emission from electrodes (stainless steel and/or niobium) could be significantly reduced and sometimes completely eliminated, by introducing krypton gas into the vacuum chamber while the electrode was biased at high voltage. Of all the electrodes tested, a large-grain niobium electrode performed the best, exhibiting no measurable field emission (< 10 pA) at 225 kV with 20 mm cathode/anode gap, corresponding to a field strength of 18.7 MV/m.

5.1 RESULTS: FIELD EMISSION VERSUS VOLTAGE (I-V CURVES)

A total of eight electrodes were evaluated – two each of DPP 304 stainless steel, fine-grain niobium, large-grain niobium and single-crystal niobium. Some electrodes were evaluated more than once, i.e., the electrode was evaluated and then removed from the apparatus and inspected. If the electrode was exhibiting field emission at low voltage/field strength, sometimes it was re-polished and the preparation steps repeated. If the electrode performed well, sometimes it was simply re-installed in the apparatus and re-evaluated. Upon initial application of high voltage, results were not always identical.

It seems plausible that the variability of initial results for the same electrode can be attributed to contamination on the electrode surface. Typically, reproducible results were obtained following patient high voltage conditioning and krypton-processing. More puzzling is the observation that results sometimes varied between electrodes of the same type. These variations might be a result of dissimilar surface finish or material imperfections present in one sample but not the other.

The field emission characteristics of the best electrode of each type are shown in Fig. 5.1.1 These I-V curves show field emission as a function of bias voltage and gap. The large-grain niobium performed the best, with no measureable field emission (< 10 pA) at 225 kV for all gaps tested. It is particularly noteworthy that this sample required no krypton processing. This sample was removed from the apparatus, inspected using an optical profilometer at another facility and re-evaluated, with the same result.

The single-crystal niobium sample performed nearly as well at large-grain niobium. Fine-grain niobium performed the worst, with only modest improvement from krypton processing. DPP stainless steel exhibited the most variability in performance. The DPP stainless steel electrodes were tested multiple times and frequently, exhibited no field emission at 225 kV and 50 mm gap. However, frequently during evaluation at smaller gaps and larger fields, the electrode would begin to field emit. Krypton processing could usually restore good performance but often, the cycle of good-to-bad performance would repeat when evaluation at smaller gaps was revisited.
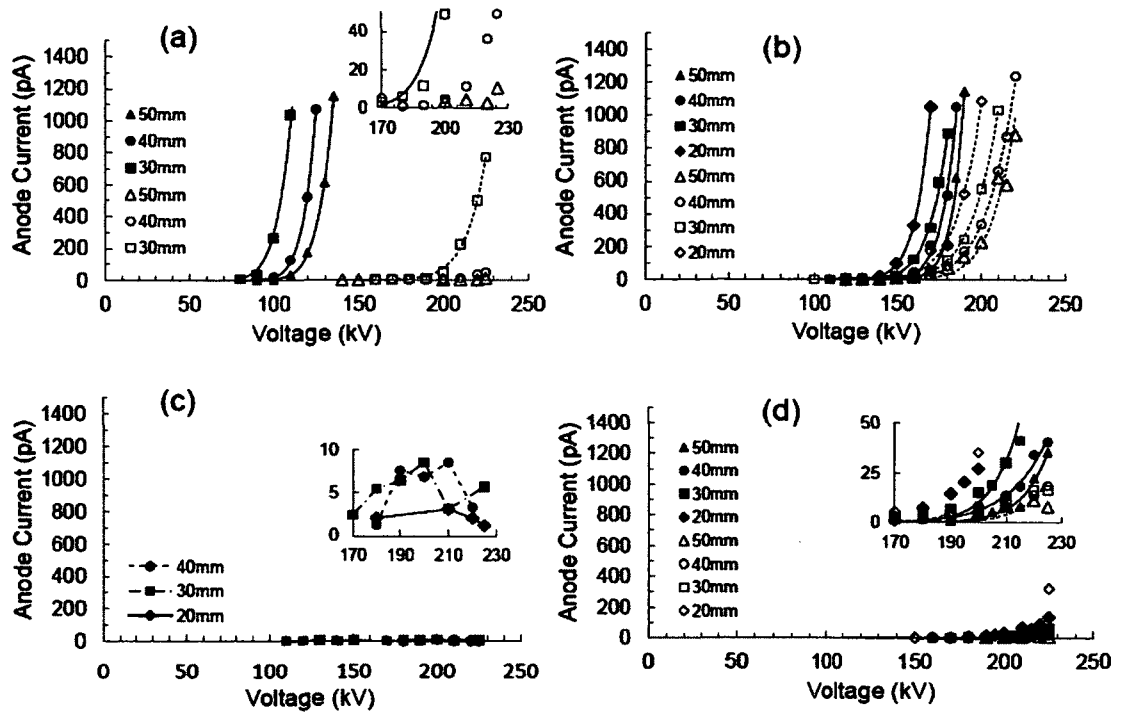
Fig. 5.1.1. Field emission current versus bias voltage and anode/cathode gap spacing for a) DPP stainless steel, b) fine-grain Nb, c) large-grain Nb and d) single-crystal Nb. Each plot shows field emission behavior before (solid symbols) and after (open symbols) krypton processing, except for large-grain Nb which did not require krypton processing. Insets show an enhanced view of the low current data points. For all cases except large-grain Nb, the lines between data points represent Fowler-Nordheim fits.

Field emission versus field strength(I-E Curves)

The field emission results of each electrode in terms of their field strength is shown in Fig. 5.1.2 and the field strength at which each electrode exhibited 100 pA of field emission current is shown in Table 5.1 and plotted as a function of gap in Fig. 5.1.3. The value 100 pA was chosen because it would have a noticeable negative impact on GaAs photocathode lifetime if it were present in a photogun, and it was enough field emission to accurately apply the Fowler-Nordheim fit to the data. Table 5.1 and Fig. 5.1.2 include results from all the electrodes, not just the best performers that were highlighted in Fig. 5.1.1. For entries with (>) symbol, field emission current did not exceed 100 pA at 225 kV bias voltage, the maximum voltage available. Consequently, the strength required to

produce 100 pA field emission must exceed the highest field accessible for the stated gap (red line in Fig. 5.1.3).

The black lines connecting data points in Fig.5 are simple power-law fits to aid the eye and do not represent a functional form associated with a specific mathematical model of field emission. For some of the electrodes – fine grain niobium, in particular - the onset of field emission occurred at higher field strengths when the cathode/anode gap was small. This behavior is representative of the trends observed by Furuta et.al., [81]. But for other electrodes, the onset of field emission was fairly insensitive to gap, and even trended in the opposite manner, with the onset of field emission occurring at lower field strengths for small gaps. These differing trends are important from a practical point of view and likely speak to interesting physics, but are not well understood.
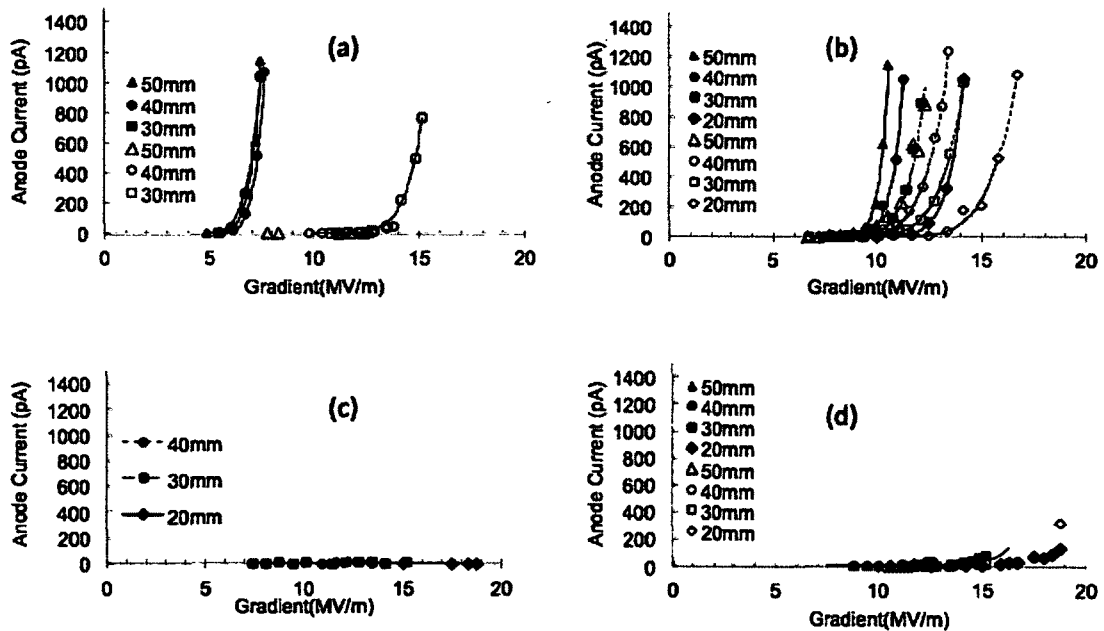
Fig. 5.1.2. Field emission current versus field strength and anode/cathode gap spacing for a) DPP stainless steel, b) fine-grain Nb, c) large-grain Nb and d) single-crystal Nb. Each plot shows field emission behavior before (solid symbols) and after (open symbols) krypton processing, except for large-grain Nb which did not require krypton processing. Insets show an enhanced view of the low current data points. For all cases except large-grain Nb, the lines between data points represent Fowler-Nordheim fits.

	FGNb1	FGNb2	SCNb1	SCNb2	LGNb1	LGNb2	DPP-SS1	DPP-SS2
50mm	11.8	10.7	>12.6	>12.6	>12.6	>12.6	>12.6	10.7
40mm	11.5	11.2	>13.8	>13.8	>13.8	>13.8	>13.8	10.0
30mm	10.8	12.0	>15.0	13.1	>15.0	15.0	13.6	9.9
20mm	10.4	14.1	>18.7	12.3	>18.7	17.5	No data	No data

Table 5.1. The field strength required to produce 100 pA of field emission, following krypton processing. For entries with (>) symbol, field emission current did not exceed 100 pA at 225 kV bias voltage, the maximum voltage available.
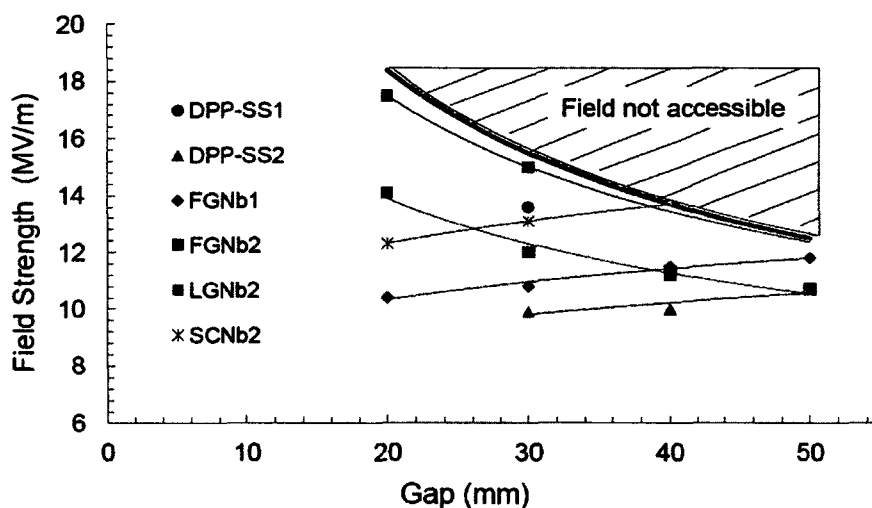
Fig. 5.1.3. The field strength at which each electrode exhibited 100 pA of field emission as a function of anode/cathode gap. For LGNb1 and SCNb1, the gfield exceeded values denoted by the red line for all gaps. For LGNb2, SCN2 and DPP-SS1, the field exceeded values above the red line at 40 and 50 mm gaps. Black lines represent simple power-law fits to aid the eye.

5.2 DISCUSSION: FOWLER-NORDHEIM ANALYSIS

The I-V curves were re-plotted using the Fowler-Nordheim line plot representation to determine the field enhancement factor β. Fig. 5.2 shows a typical line plot result, before and after krypton processing, for large-grain niobium. The benefit of krypton processing is dramatically evident, with a reduction in β from 368 to 173. Table 5.2.1

summarizes the field enhancement factors for all electrodes that exhibited sufficient levels of field emission. For these calculations, a work function of 4.3 eV was used for all forms of niobium, and 4.5 eV for stainless steel. For most of the entries in Table 5.2, the field enhancement factor was constant to within 5 to 20 % for each gap. There are a few examples where the field enhancement factor of an electrode varied markedly at a particular gap, suggesting the birth of a new field emitter. In hindsight, further processing was likely required.

Two electrodes (single-crystal Nb1 and large-grain Nb1) did not exhibit enough field emission to apply the Fowler-Nordheim functional fit to the data. For these electrodes, β can be assumed to be smaller than values measured for the other electrodes. The field enhancement factor for all electrodes decreased significantly following krypton processing, with one exception (fine-grain Nb2) and this anomaly is not understood. It is common to assume β to be proportional to the ratio of the height of the emitter to the radius of the emitter. Large β values describe tall protrusions, and/or protrusions with small radius. It is reasonable to assume that krypton processing can reduce the height of emitters due to ion bombardment, with emitter material sputtered away. In this view, it difficult to understand how krypton processing could increase the size of the field enhancement factor for fine-grain Nb2.
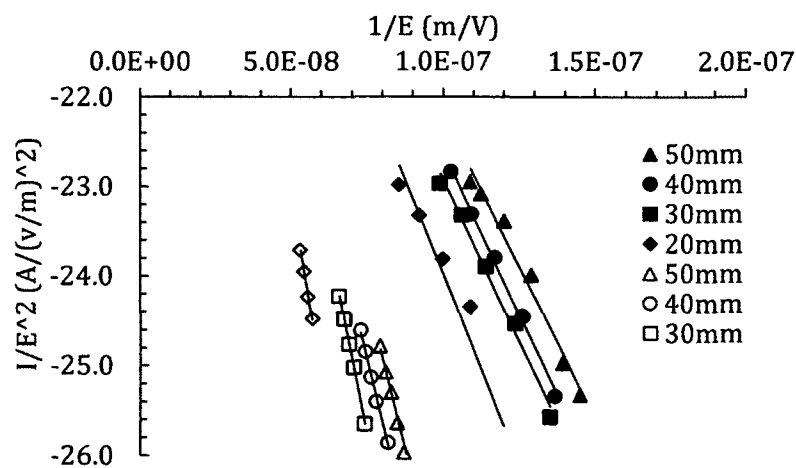
Fig. 5.2. Example of Fowler-Nordheim line plots for large-grain niobium before (solid symbols) and after (open symbols) krypton processing.

Pre Krypton	50 mm	40 mm	30 mm	20 mm	Avg
FGNb1	696	738	764	743	735
FGNb2	394	328	261	268	313
SCNb1 *	-	-	-	-	-
SCNb2	615	565	494	454	532
LGNb1 *	-	-	-	-	-
LGNb2	399	375	377	320	368
DPP-SS1	754	670	703	No data	709
DPP-SS2	1118	796	1156	No data	1023

Post Krypton	50 mm	40 mm	30 mm	20 mm	Avg
FGNb1	263	387	260	268	295
FGNb2	687	698	648	478	628
SCNb1 *	-	-	-	-	-
SCNb2	349	490	231	232	326
LGNb1 *	-	-	-	-	-
LGNb2	205	196	156	136	173
DPP-SS1	214	684	301	No data	400
DPP-SS2	394	279	276	No data	316

(*)   Beta could not be determined for these electrodes because there was too little field emission to provide an accurate Fowler Nordheim line-plot fit.

Table 5.2.1. shows β-values for all eight electrodes, before and after krypton processing.

As mentioned previously, the y-axis intercept of the Fowler-Nordheim line plot is related to the surface area of the field emitter. Emitter area values are shown in Table 6.2.2. All of the emitter area values are extremely small, especially considering that ref. 23 predicts typical field emitter areas $10^{-16} < A_e < 10^{-12}$ m^2. This is likely an indication that field emission originates from multiple locations whereas traditional Fowler-Nordheim theory assumes just one emitter. In addition, Table 3 indicates that emission area increases following krypton processing. This might be explained by krypton ions

sputtering away sharp tips, making them more rounded, or blunt. It might also be related to a greatly reduced number of field emitters contributing to the total measured current.

	FGNb1	FGNb2	SCNb1*	SCNb2	LGNb1*	LGNb2	DPP-SS1	DPP-SS2
Intercept Pre Kr	-17.8	-15.8	-	-18.5	-	-15.5	-17.6	-18.3
Intercept Post Kr	-15.5	-20.3	-	-17.4	-	-13.7	-22.6	-15.4
A_e Pre Kr	6.8E-20	2.1E-16	-	8.1E-20	-	4.5E-17	1.1E-19	7.7E-20
A_e Post Kr	5.1E-16	2.6E-22	-	2.1E-16	-	5.3E-14	4.6E-19	8.6E-16

(*) Information could not be determined for these electrodes because there was too little field emission to provide an accurate Fowler Nordheim line-plot fit.

Table 5.2.2. Fowler-Nordheim line plot intercept values and emission areas, assuming all of the field emission originates from a single emitter.

5.3 OPTICAL PROFILOMETER IMAGES AND SURFACE ROUGHNESS

After characterizing field emission performance in the high voltage test apparatus, each electrode was studied using an optical profilometer [82], to look for obvious field emitters and to determine surface roughness. An optical profilometer does not contact the surface of the specimen under investigation. Two roughness numbers are reported for each electrode in Table 5.3, one quantity describes a periodic large-scale roughness (or waviness) and the other quantity describes roughness on a fine scale. The same profilometer data file was used to determine both quantities but using different spatial filtering. The periodic roughness/waviness was determined by applying a low-pass filter to the data file, to eliminate fine-scale variations, and is therefore somewhat subjective. Waviness originates from the machining process and relates to how fast the cutting tool was moved across the electrode during fabrication. The fine scale roughness quantity is considered to be the more relevant metric when considering field emission.

False-color images of representative electrodes are shown in Fig. 5.3.1. Each image represents a portion of the electrode near the crown, in the vicinity of the region exposed to high field. Fine-grain niobium had the roughest surface finish (200 to 300 nm), and perhaps not surprisingly exhibited the highest levels of field emission. Single-

crystal niobium and DPP stainless steel electrodes had the smoothest surface finish (10 to 20 nm) and interestingly single-crystal niobium performed very well whereas DPP stainless steel frequently exhibited high levels of field emission. Perhaps most surprisingly, large-grain niobium had mid-level roughness but exhibited the lowest levels of field emission. Good performance despite a rough surface could be due to a "screening effect" that serves to reduce the field enhancement factor β [83]. Beneficial screening requires that field emitter protrusions occur on the surface of the electrode with the correct spatial periodicity. This is illustrated in Fig. 5.3.2, showing images of both large-grain Nb electrodes. Large-grain niobium1 exhibited a rough surface composed of closely spaced ridges and this likely proved fortuitous - the spacing of the ridges presumably served to reduce the effective height of individual ridges, with only a shallow penetration of field lines between ridges.

Table of roughness

	FGNb1	FGNb2	SCNb1	SCNb2	LGNb1	LGNb2	DPP-SS1
Roughness (nm)	303.95	215.1	17.6	10.2	141.01	51.98	10.9
Waviness (nm)	545.4	565.5	71.1	107.7	452.6	372.1	25.3

Table 5.3. Surface roughness values of all electrodes obtained using an optical profilometer.
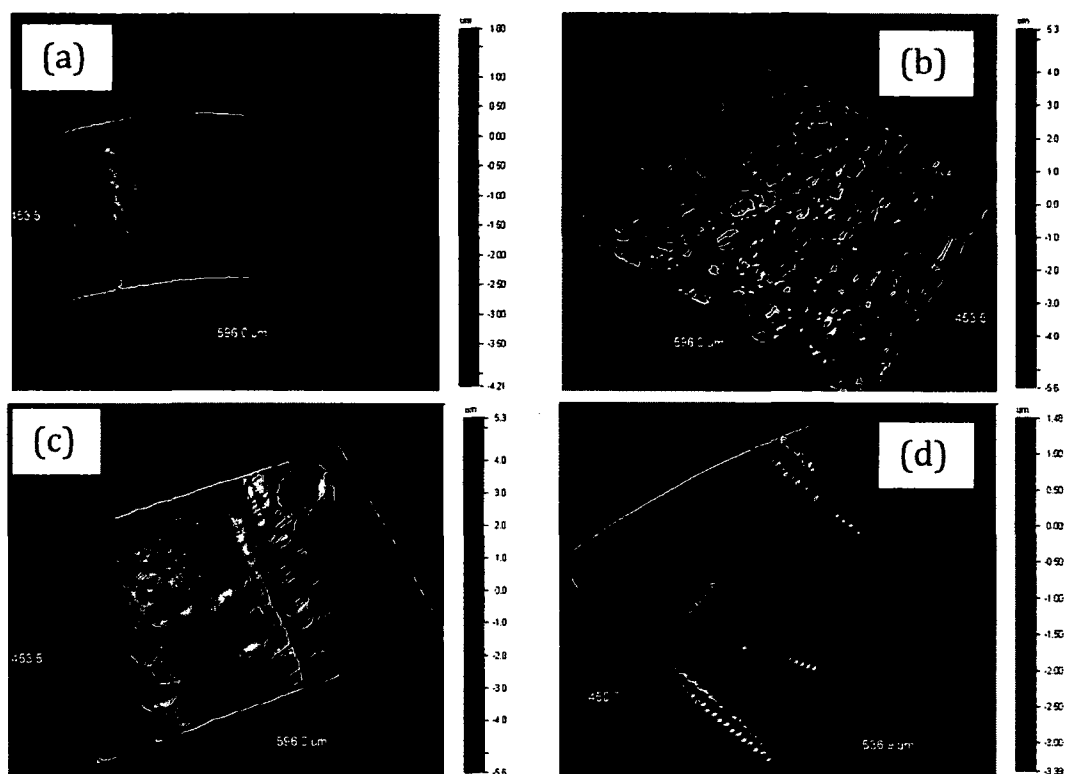
Fig. 5.3.1. Optical profilometer images of: a) DPP 304 stainless steel, b) fine-grain niobium, c) large-grain niobium and, d) single-crystal niobium. The span of each image is very nearly the same, approximately 450 μm x 600 μm
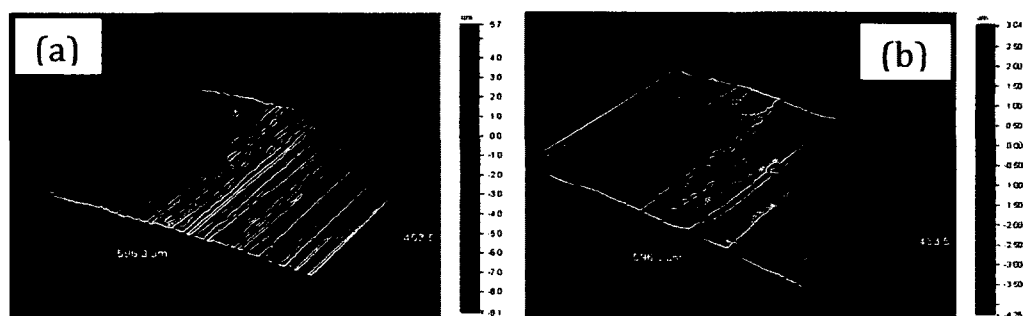
Fig. 5.3.2. Optical profilometer images of both large-grain niobium electrodes: a) sample#1 with surface roughness 141 nm, and b) sample#2 with surface roughness 52 nm. Large-grain niobium sample#1, with rougher surface, performed the best.

The surface of some of electrodes – in particular large-grain and single-crystal niobium – exhibited shallow craters. An iterative profilometer analysis of a large-grain niobium electrode indicated that the craters were not visible before the application of high voltage, and the craters were not a result of krypton processing. As such, a crater is likely an indication of a field emission site (either active or inactive). Typical crater dimensions are 20 to 50 μm diameter and 0.2 to 1 μm deep. The crater pattern for large-grain niobium was random although frequently, craters were centered on the top of ridges. For single-crystal niobium, craters appeared along lines that indicate the presence of micro-scratches. Similar craters might be present on the surface of fine-grain niobium but indistinguishable due to scale of the grain boundaries of these materials. No craters were visible for DPP stainless steel.

The surface features of the eight test electrodes described above are significantly larger than the emitter area dimensions predicted by the Fowler-Nordheim line plot analysis (Table 3), which supports the notion that for large smooth electrodes, the observed field emission is likely a result of multiple field emitters. To test the validity of this assertion, a third DPP stainless steel electrode with a known field emitter – or more plainly, an electrode with a clearly defined scratch – was evaluated in the field emission test stand. The scratch was 70 nm "tall" (peak to valley) and 1.1 cm long. As expected, field emission was observed at low voltages and field strength and a Fowler-Nordheim line plot analysis of the results indicated a field enhancement factor of 444 and emitting area of 2.3e-10 m^2. The field enhancement factor β is also frequently defined as the ratio of emitter height to emitter radius. Using the β -value from the Fowler-Nordheim line plot analysis and the emitter height value from the AFM measurement, the emitter radius was estimated to be 0.16 nm. The radius and the length of the scratch can be used to estimate the geometric area of the emitter ($A_e = \pi \cdot r \cdot l$), or 5.5e-12 m^2. So although the two values for A_e differ by a factor of 42, this is considerably better agreement compared to the emitter area assessment of large smooth electrodes. This suggests that when field emission originates from a single emitter, a Fowler-Nordheim line plot analysis can provide quantitative insight into the physical characteristics of the emitter.

5.4 CONCLUSION

Large-grain niobium appears to be excellent choice for manufacturing electrodes for DC high voltage photoguns, reaching higher voltages and field strengths without field emission, compared to diamond-paste polished stainless steel. One sample of large-grain niobium performed the best, reaching 225 kV and 18.7 MV/m without measurable field emission. This electrode performed well during initial testing and upon repeated re-evaluation. Large-grain niobium is readily available, for example compared to single-crystal niobium, which also performed well. In contrast, "reactor grade" fine-grain niobium with RRR value ~ 40 exhibited comparatively high levels of field emission. Fine-grain niobium with RRR value > 250 will be evaluated in the future. All of the niobium electrodes were prepared in less time compared to DPP-stainless steel electrodes.

Sometimes, results varied significantly for the same electrode and/or for different electrodes of the same material. This variability complicates the process of assigning firm conclusions. The performance of an electrode could be improved significantly via krypton processing. It seems reasonable to assume krypton processing served to eliminate field emission stemming from random contamination. Besides providing a very practical means to reduce field emission from an electrode, the authors feel that krypton-processing served as a useful tool to reduce the variability in field emission results.

A traditional Fowler-Nordheim line plot analysis of the field emission results was easy to perform but of marginal practical value, largely because the Fowler-Nordheim theory assumes a single field emitter and for large electrodes, this does not seem to be realistic.

Optical profilometry indicated that a smooth surface does not guarantee cathode performance free of field emission however it did provide a possible explanation for why one large-grain niobium electrode performed better than the other electrode, namely a surface with periodic structure served to lower the field enhancement factor via a process termed screening. Optical profilometry also provided useful information related to the physical characteristics of field emission sites (i.e., dimensions), although it is not known if the observed crater-like structures on the surface of large-grain and single-crystal niobium electrodes represent active or inactive field emission sites.

CHAPTER 6

EVALUATION OF ELECTROPOLISHED STAINLESS STEEL ELECTRODES

FOR USE IN DC HIGH VOLTAGE PHOTOELECTRON GUNS

Three stainless steel cathode electrodes with different initial surface roughness were electropolished by a commercial vendor, and evaluated inside a high voltage test stand capable of operation at -225kV and field strength $\sim$ 18 MV/m. Upon the initial application of voltage, the electropolished electrodes exhibited less field emission compared to two of three electrodes that were mechanically polished with silicon carbide paper and diamond grit, but unlike diamond-paste polished electrodes, the performance of the electropolished electrodes did not improve following gas conditioning. For a cathode/anode gap of 50 mm, the diamond-paste polished electrodes showed no field emission at - 225 kV and field strength $\sim$ 13 MV/m whereas electropolished electrodes exhibited field emission at negative voltages in the range of 130-160 kV and at field strengths between 8 and 10 MV/m. The electropolished electrodes had rough surfaces at low spatial frequencies compared to diamond paste polished electrodes, which could explain their comparatively poor performance. And simulation results suggest rough surfaces are less receptive to ion implantation, which could explain why gas conditioning did little to improve the performance of the electropolished electrodes.

6.1   Introduction

One of the limiting factors of DC high voltage electron guns is field emission from the cathode electrode which degrades the vacuum near the gun. Field emission is especially problematic for DC high voltage photoguns where poor vacuum conditions lead to rapid decrease in photocathode yield, but even thermionic guns suffer reduced lifetime in the presence of field emission. The onset of field emission sets the acceptable operating voltage of the electron gun, sometimes restricting operation at voltage significantly below the desired value. Recently, there is a tremendous desire to operate electron guns at very high voltages, $\sim$ 500kV [84, 90], and eliminating field emission has been the key technological challenges.

Except following the field emission elimination techniques like gas conditioning [91], choosing the right surface polishing techniques can be field emission preventive as well. Surface particulates and irregularities are very important sources of enhanced field emission that need to be overcome in order to increase the efficient performance of DC photo guns. These sources appear in two different forms; as micro protrusions or as adhered miro-particles that can enhance the electric discharge from the surface and result in to the gap insulation breakdown between the electrodes. Surface treatments are one of the very important parts of field emission reduction process to obtain the surface free of sources of discharge .

In 1969 Owen et [92] all observed that different cathode surfaces with the same anode electrode, affects the break down voltage. Williams and Williams in 1972 [93] evaluated the relative effectiveness of different polishing techniques like machining, diamond paste polishing and electro-polishing on field emission current and electrical breakdown voltage. He found "mechanical polishing" to be the most reliable technique providing the most stable field emission current.

It is common to polish the electrodes used inside electron guns to mirror-like surface finish using silicon carbide paper and diamond paste of successively finer grit. However, diamond-paste polishing is a time consuming process requiring strict adherence to protocol [91], with prevailing wisdom suggesting that pressing too hard on the piece leads to microscopic tips that become "rolled over", and as a result, trapping particulate contamination. As a result, the performance of one diamond-paste polished electrode can be very different from that of another that was polished, for example, by another person. There is strong interest in developing polishing procedures that provide consistent and favorable results, and ideally, requiring less time and labor.

Electropolishing is a widely used technique to smooth metallic surfaces, for example to reduce the surface area of vacuum chambers and thereby reduce the gas load due to hydrogen outgassing [94]. A number of photogun groups have tested electropolished electrodes inside DC high voltage photoguns, however field emission remains a significant problem preventing operation at 500 kV [95, 96].

During electropolishing, the piece to be polished is immersed in an electrolytic bath, typically acid, and biased positive. A nearby sacrificial electrode is biased negative and current passes between the two electrodes. The surface of the piece being polished becomes oxidized and this oxide layer dissolves away. For the process to be successful, the protrusions at the surface must dissolve faster than the recesses. A number of important parameters can influence the efficacy of electropolishing, including the temperature of the electrolytic bath, the types and concentration of acids used, and the rate at which the solution passes across the work piece surface. For this work, the electrodes were electropolished by a commercial vendor [97], using a proprietary process, but one considered to be relatively generic in terms of the technique. Electropolishing resulted in the removal of approximately 10 μm of material from the surface.

Three stainless steel (316L) cathode electrodes with different initial surface roughness were electropolished. These electrodes were then sequentially evaluated inside a high voltage test stand to determine the onset of field emission as a function of voltage and field strength. The performance of these electrodes was compared to that of electrodes polished using silicon carbide paper and diamond grit. All of the electrodes were evaluated before and after gas conditioning. Electropolished electrodes exhibited less field emission upon the initial application of high voltage, however they showed less improvement with gas conditioning. The diamond-paste polished (DPP'ed) electrodes ultimately reached higher voltages and field strengths without field emission, following gas conditioning, compared to electropolished (EP'ed) electrodes. An assessment of electrode surface finish using multiple techniques indicates that electropolished electrodes have significantly more coarse-scale roughness compared to diamond-paste polished electrodes. Simulation results indicate that less ion implantation occurs on rough surfaces, possibly explaining why EP-ed electrodes do not exhibit improvement following gas conditioning.

6.2   EXPERIMENT DESCRIPTION

A total of six electrodes were evaluated at high voltage as part of this study. Each Pierce-type electrode with a 25 degree focussing angle (6.35 cm dia., 2.85 cm thick) had a shape identical to electrodes used inside a DC high voltage photogun employed at the Continuous Electron Beam Accelerator Facility at Jefferson Lab [98]. Electrodes were manufactured from 304L and 316L stainless steel and cut to shape using hydrocarbon-free lubricants to obtain a 32 micro-inch RMS surface finish.

Diamond Paste Polishing of Stainless Steel

Diamond-paste polishing is a conventional polishing technique employed for many decades, particularly for electrodes used inside DC high voltage photoelectron guns. Symmetric electrodes were polished on a potter's wheel, first with silicon carbide paper of increasingly finer grit (300 and then 600 particles/in^2) followed by polishing with diamond grit (6 µm and then 3 µm). Between each polishing step, the electrode was cleaned in an ultrasonic bath using an alkali solution. The end result is an electrode with mirror-like surface finish.

Electropolishing of Stainless Steel

As mentioned previously, electropolishing provides a smooth surface when surface protrusions are dissolved faster than surfaces within recesses. One goal of the study was to determine the optimum initial surface finish prior to electropolishing. To this end, three electrodes were electropolished but with different initial surface finish: one electrode was electropolished immediately following machining, one after mechanical polishing with silicon carbide paper (300 and 600 particles/in^2), and one after silicon carbide polishing (300 and 600 particles/in^2) and diamond-paste polishing (6 and 3 µm grit). The amount of labor required to prepare these electrodes prior to electropolishing varied significantly, from minutes to many hours.

The surface roughness of each electrode was evaluated using an optical profilometer [99] with false-color images shown in Figure 6.2.1. Each image shows a portion of the electrode near the crown, in the vicinity of the region exposed to highest

field strength, and therefore the region most likely to produce field emission. The top row shows images of the electropolished electrodes labeled EP1, EP2 and EP3 and the bottom row shows images of diamond-paste polished electrodes labeled DPP1, DPP2 and DPP3. Surface roughness (a quantity describing fine scale variations) and waviness (a quantity describing periodic large-scale variations) are summarized in Table 6.2. Overall, the electropolished electrodes exhibit higher levels of large and fine scale roughness compared to diamond-paste polished electrodes. It was surprising that the electrode polished with silicon carbide paper before electropolishing (EP2), exhibited comparable surface features as the electrode that was electropolished without any preparatory mechanical polishing (EP1). It should be mentioned that the electrode that was diamond-paste polished and then electropolished (EP3), was first characterized as DPP1, and that electropolishing served to slightly elevate the fine and coarse-scale roughness of this electrode.
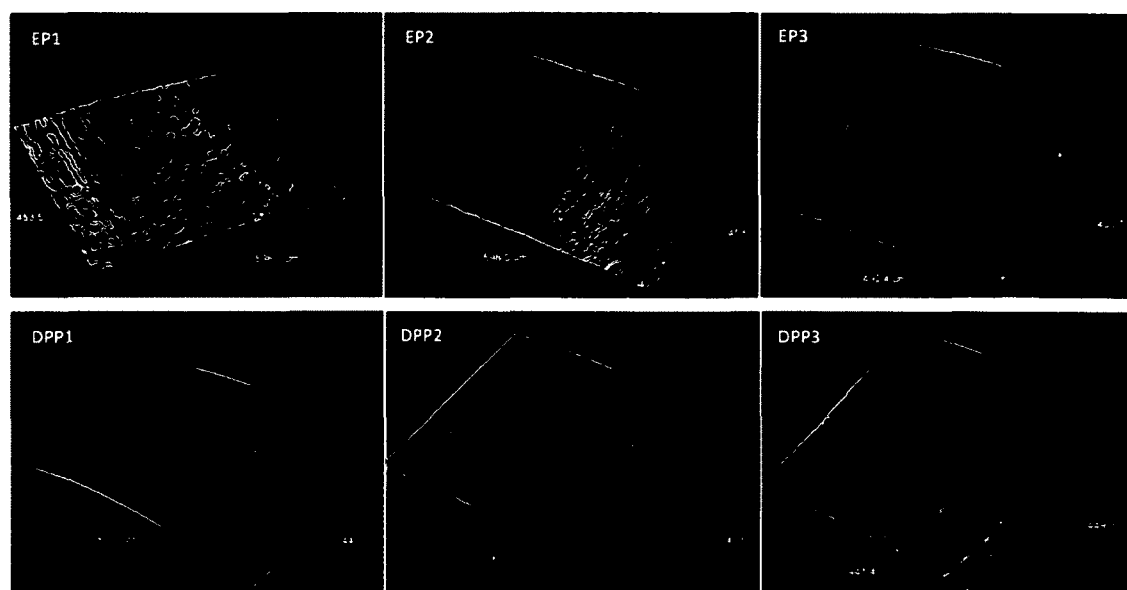

Fig. 6.2.1. Optical profilometer images of the electrodes showing regions near the crown, in the vicinity of the highest field strength. Top) electropolished electrodes. Bottom) diamond-paste polished electrodes. Specific details of each electrode are described in the text.

	EP1	EP2	EP3	DPP1	DPP2	DPP3
Waviness (nm)	312	385	28	25	30	73
Roughness (nm)	163	140	17	11	29	31

Table 6.2. Surface variations of six electrodes measured using an optical profilometer, on a fine and coarse scale (roughness and waviness, respectively). Electrode EP3 was originally electrode DPP1.

Cathode electrodes were attached to a tapered conical insulator that extends inside an ultrahigh vacuum test chamber (Fig. 6.2.2). The same stainless steel (304L) anode was used for all measurements, and consisted of a flat plate with a Rogowski edge profile that was electrically isolated from ground and attached to a sensitive current meter (Keithley electrometer model 617). The anode could be moved up or down to vary the cathode/anode gap and therefore the field strength. The anode was polished with 600 particles/in^2 silicon carbide paper and 6 $\Box$m diamond grit.

Prior to the application of high voltage, the entire vacuum apparatus was baked at 200°C for 30 hours to achieve vacuum level in the 5x10^{-11} Torr range. Every effort was made to keep the vacuum conditions consistent from sample-to-sample. A full description of the test apparatus can be found in reference 8.
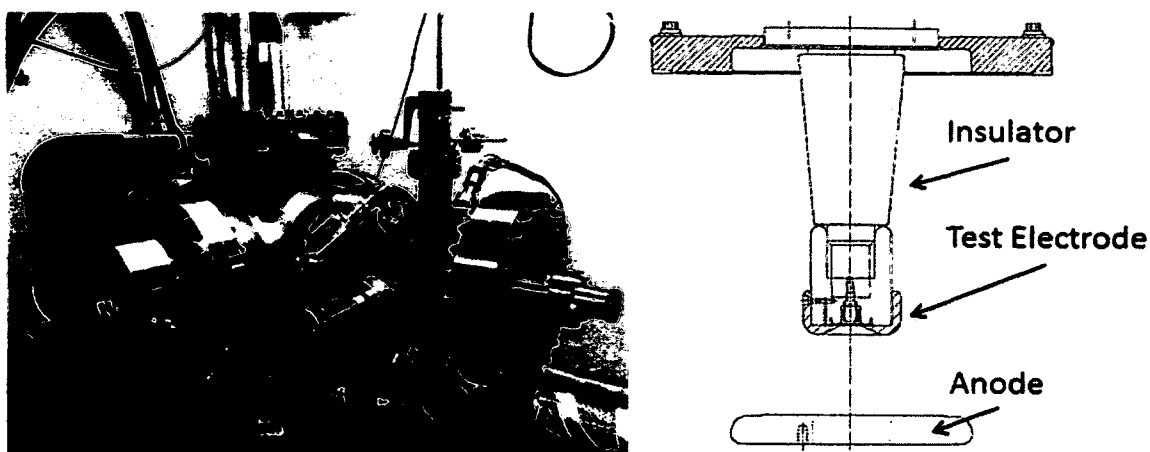
Fig. 6.2.2. Photograph of the dc high voltage field emission test stand used to evaluate each cathode electrode (left), a schematic view of the insulator, test electrode and anode used to collect the field emission (right).

6.3 Experimental Results

Electrodes were first evaluated following "current conditioning" [100], a technique where voltage is applied gradually and in small incremental steps, with field emission sites sometimes "burning off" and becoming more stable. However, current conditioning is considered an unpredictable method that sometimes results in high voltage breakdown, leading to electrode damage and necessitating repolishing.

Following relatively cautious current conditioning, electrodes were evaluated a second time after "gas conditioning" [91], a technique where gas is introduced into the vacuum chamber while the cathode electrode is biased at a voltage high enough to produce field emission. The gas becomes ionized, with ions accelerated toward the cathode electrode, ideally striking the electrode in the vicinity of the field emitter. These back-accelerated ions eliminate field emission via sputtering and/or implantation which serves to increase the work function of the surface. Two gasses were used in these experiments, helium and krypton, at pressure $\sim 1 \times 10^{-5}$ Torr, and for 30 minute intervals. Inert gasses were chosen because the non-evaporable getter pumps inside the vacuum apparatus do not pump inert gas: when the supply of gas was terminated, the vacuum level quickly recovered to a level nearly the same as before gas conditioning. As will be

described further below, sometimes improved performance was observed in just one implementation of gas conditioning. Sometimes multiple conditioning cycles were implemented. The two gasses with distinctly different atomic mass provided some control over the two conditioning mechanisms sputtering and implantation.

Electrode evaluation involved monitoring the vacuum level via the ion pump current, x-ray radiation with Geiger monitors placed around the apparatus, and the anode current with a digital electro-meter, while increasing the applied voltage. High voltage was first applied to the electrode using the largest cathode/anode gap of 50 mm where the maximum field strength reaches 13 MV/m at -225 kV bias. The gap was then decreased to achieve higher field strength. The smallest gap used for these tests was 20 mm and provided maximum field strength of ~ 18 MV/m when the cathode was biased at -225 kV. Smaller gaps provided significantly higher field strength, but sometimes produced catastrophic breakdown and electrode damage. To avoid damaging the electrodes, an effort was made to limit field emission current to a few nA during current conditioning and a few □A during gas conditioning.

Field emission current versus voltage is shown in Figure 6.3, for both groups of electrodes, before and after gas conditioning. The results for electropolished electrodes are displayed on the left, and on the right for diamond paste-polished electrodes, with solid lines and closed markers representing results before gas conditioning, and dashed lines and open markers representing results post-gas conditioning. Surprisingly, despite the large variation in roughness characteristics, the results for all three electropolished electrodes are very similar, with field emission observed to "turn ON" at voltage between 110 and 150 kV for all gaps. Interestingly, inert gas conditioning did very little to improve the performance of the electrodes, and in the case of EP1, actually served to degrade performance. In comparison, the diamond-paste polished electrodes exhibited large variations in performance before gas conditioning, with two of the electrodes producing field emission at voltage less than 100 kV. All three diamond-paste polished electrodes improved significantly following gas conditioning, achieving comparable performance and showing no field emission at -225 kV and at a 50 mm gap.
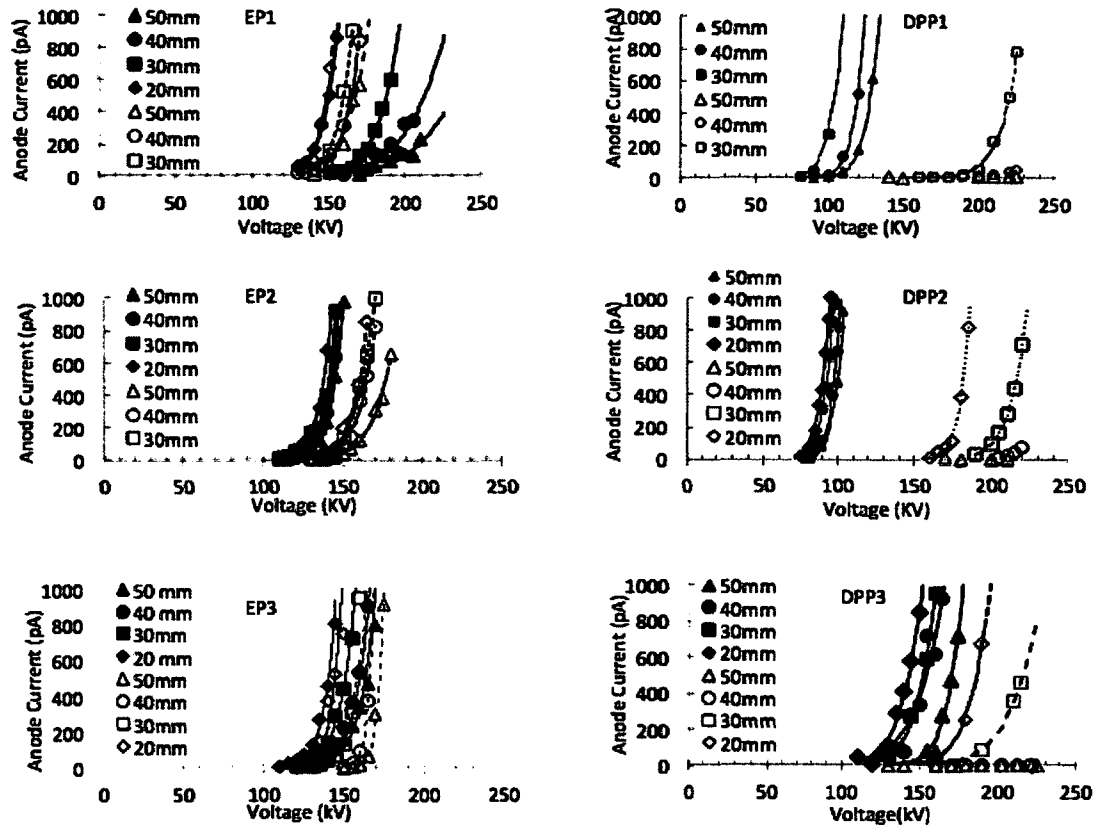
Fig. 6.3. I to V curves: field emission versus applied voltage for electrolished electrodes (left) and diamond-paste polished electrodes (right). Solid lines and closed markers represent results before gas conditioning, dashed lines and open markers represent results post-gas conditioning. The lines represent fits to the data using Fowler-Nordheim equation.

Table 6.3 lists the field strength at which each electrode produced 100 pA of field emission for anode/cathode gaps between 20 and 50 mm. Field strength values were estimated using the field mapping program POISSON [64]. The value 100 pA was chosen because it was large enough to accurately apply a Fowler-Nordheim fit to the data. Before gas conditioning, the electropolished electrodes reached higher field strengths before field emitting, compared to diamond-paste polished electrodes: electropolished electrodes reached field strengths of 8 to 11 MV/m compared to 5 to 9

MV/m for diamond paste polished electrodes. However, after gas conditioning, the diamond-paste polished electrodes improved significantly, reaching field strengths greater than ~ 13 M/m without field emission, whereas the performance of the electropolished electrodes was unchanged, or slightly worse.

Turn on Field Strength (MV/m) at 100pA , Before/After Gas Conditioning vs. Gaps

Gap(mm)	Pre-Conditioning			Post-Conditioning		
	EP1	Ep2	EP3	Ep1	EP2	EP3
50	10.9	7.3	8	8.2	9.2	9.5
40	11.1	8.1	8.7	9.1	9.9	9.8
30	11.4	8.7	9.4	9.8	10.5	10
20	11.3	10.5	10.7	11.3	12.8	11

Turn on Field Strength (MV/m) at 100pA , Before/After Gas Conditioning vs. Gaps

Gap(mm)	Pre-Conditioning			Post-Conditioning		
	DPP1	DPP2	DPP3	DPP1	DPP2	DPP3
50	6.4	4.9	8.7	>12.6	>12.6	>12.6
40	6.6	5.4	8.1	>13.8	>13.8	>13.8
30	6.2	5.5	9.1	13.6	13.5	12.9
20		6.6	10.5		14.4	14.1

Table 6.3. The field strength (MV/m) at which each electrode exhibited 100 pA of field emission at different gaps before and after gas conditioning. Top: electropolished electrodes. Bottom: diamond paste polished electrodes. For entries with (>) symbol, field emission current did not exceed 100 pA at -225 kV, and consequently, the field strength must exceed the maximum value provided by the high voltage power supply.

6.4 DISCUSSION

Optical profilometry provides a useful measure of fine and coarse scale roughness, however there is a level of subjectivity associated with this evaluation technique, with just a small portion of the total surface area studied and also due to filtering software that can be adjusted by the user. Significantly more information can be gleaned from power spectral density plots which show relative contributions of roughness evaluated over a very large range of spatial frequencies. Specifically, a power spectral density plot shows the squared amplitude of surface features plotted versus spatial frequency. Power spectral density plots were obtained by making 50 x 50 μm^2 acetate "negatives" of the electrode surface, which were then analyzed using an atomic force microscope [101, 102]. The power spectral density plots of five electrodes (EP1, EP2, DPP1, DPP2, DPP3) are shown in Figure 6.4.1. These plots indicate that electropolished electrodes have rough surfaces compared to diamond-paste polished electrodes, particularly at low spatial frequencies.   Such an observation is consistent with an electropolishing procedure that was not effective at selectively removing sharp features while leaving material intact within surface recesses.
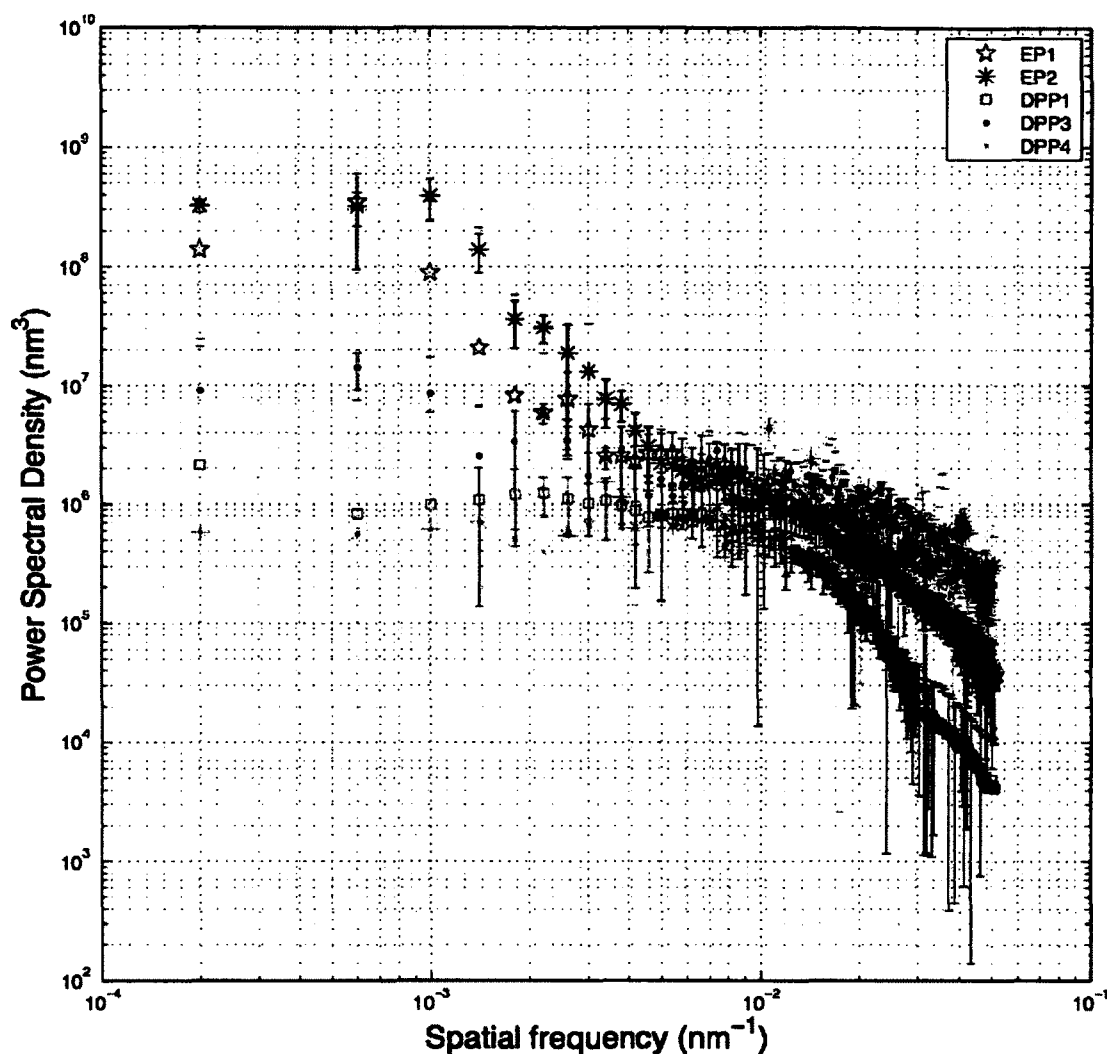
Fig. 6.4.1. Power spectral density plots of four electrodes: two electropolished and three diamond-paste polished, providing a measure of surface variation as a function of spatial frequency. The electropolished electrodes have more coarse-scale roughness.

To better appreciate how the surface conditions of the electropolished electrodes could affect the efficacy of gas conditioning, simulations were performed using the software program TRIM (Transport of Ions in Matter) [103]. Recall that gas conditioning serves to eliminate field emission as a result of sputtering, where sharp tips are made blunt, and implantation, where embedded ions serve to increase the work

function at the electrode surface. Figure 6.5.2 shows the TRIM simulation result of helium and krypton ion implantation as a function of angle of incidence (0, 45 and 90 degree), where 0 degrees corresponds to ions striking the electrode normal to the surface. For both gas species, there are significantly fewer ions implanted within the electrode at large angles of incidence, i.e., a condition representative of a rough surface.

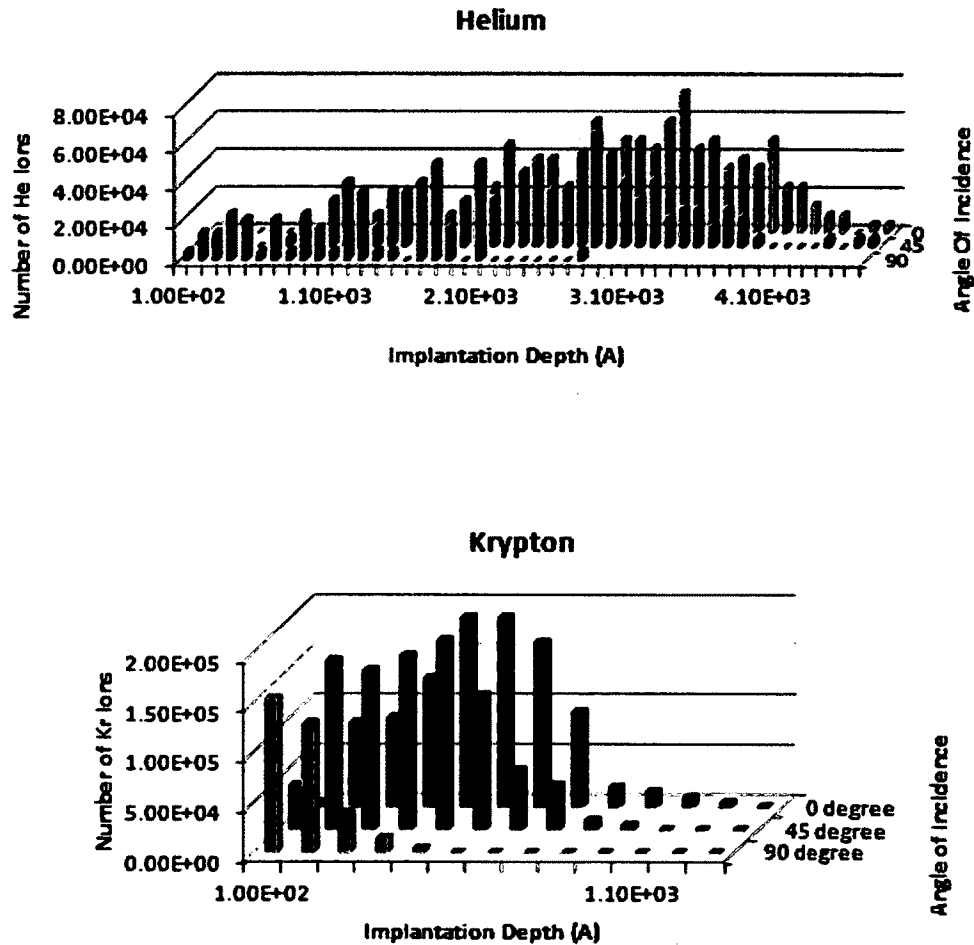Fig. 6.5.2. Top) the number of helium ions implanted within a satainless steel surface as a function of angle of incidence, with 0 degrees representing an ion striking the surface at normal incidence. Bottom) a similar plot for krypton ions.

Figure 6.5.3 shows ion sputtering from stainless steel versus the angle of incidence, for both helium and krypton, obtained using TRIM. For helium ions (top plot), the

sputtering yield is relatively constant as a function of angle of incidence, although as expected, the sputtering yield is very small compared to krypton (bottom plot). Sputtering yield for krypton is maximum at an angle of incidence of 70 degrees. As a result, sputtering from the recesses of a rough surface will be less efficient, because adjacent surface peaks restrict access to only small angles where the sputtering yield is approximately five-times smaller.
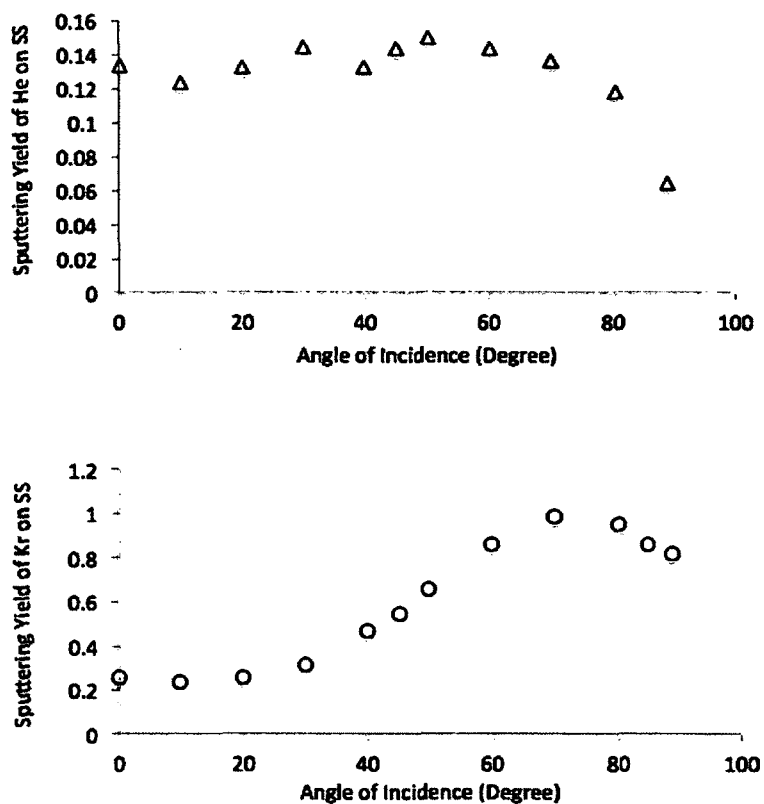
Fig. 6.5.3. Sputtering yield from stainless steel versus the angle of incidence for helium and krypton.

6.5 CONCLUSION

Upon the initial application of voltage, electropolished stainless steel electrodes reached higher voltages and field strengths without field emission, compared to diamond-

paste polished stainless steel electrodes, but ultimately, the diamond-paste polished electrodes performed significantly better than electropolished electrodes following gas conditioning. For a cathode/anode gap of 50 mm, the diamond-paste polished electrodes showed no field emission at - 225 kV and field strength ~ 13 MV/m whereas electropolished electrodes exhibited field emission at negative voltages in the range of 130-160 kV and at field strengths between 7 and 11 MV/m.

To better appreciate why electropolished electrodes did not respond favorably to gas conditioning, the electrode surfaces were evaluated using an optical profilometer and acetate negatives and an atomic force microscope. The electropolished electrodes surfaces were markedly rougher compared to diamond paste polished electrodes, and simulation results suggest there is significantly less ion implantation during gas conditioning on rough surfaces compared to smooth surfaces.

These results are consistent with other reports in literature, namely Williams and Williams in 1972 [93] evaluated the relative effectiveness of different polishing techniques including machining, diamond-paste polishing and electropolishing. They found mechanical polishing to be the most reliable technique providing the most stable field emission current. In 1985 Gruszka and Moscicka-Grzesiak [104] investigated the effects of current conditioning on electropolished stainless steel, aluminum and copper electrodes. They discovered that the emission current depends on the type of metal and the surface roughness of the electrodes. They observed that the optimum conditioning current has a greater value in case of the smoother electrode surface. This resembles the same situation in conditioning our Ep'ed electrodes. In the higher spatial frequency region, EP'ed electrodes are smoother than most of the DPP'ed ones; therefore the Ep'ed surface might still get benefits from inert gas conditioning if the limit set points for current, voltage and X-rays could be increased as observed in the Jlab FEL gun high voltage conditioning [105].

It must be noted that despite the unsuccessful gas conditioning results of EP'ed electrodes, it is possible other electropolishing recipes could provide a smoother surface, and hence better results. The potential advantages electropolishing, namely simplicity compared to diamond-paste polishing, are worth further investigation.

CHAPTER 7
FOWLER NORDHEIM BEHAVIOR OF BREAKDOWN ON FR CAVITY ELECTRODE

Microscopic images of the surfaces of metallic electrodes used in high-pressure gas-filled 805 MHz RF cavity experiments [106] have been used to investigate the mechanism of RF breakdown [107] The images show evidence for melting and boiling in small regions of ~10 micron diameter on tungsten, molybdenum, and beryllium electrode surfaces. In these experiments, the dense hydrogen gas in the cavity prevents electrons or ions from being accelerated to high enough energy to participate in the breakdown process so that the only important variables are the fields and the metallic surfaces. The distributions of breakdown remnants on the electrode surfaces are compared to the maximum surface gradient E predicted by an ANSYS model of the cavity. The local surface density of spark remnants, proportional to the probability of breakdown, shows a strong exponential de- pendence on the maximum gradient, which is reminiscent of Fowler-Nordheim behavior of electron emission from a cold cathode. New simulation results have shown good agree- ment with the breakdown behavior of the hydrogen gas in the Paschen region and have suggested improved behavior with the addition of trace dopants such as SF6 [108] Present efforts are to extend the computer model to include electrode breakdown phenomena and to use scanning tunneling microscopy to search for work function differences between the conditioned and unconditioned parts of the electrodes.

7.1 INTRODUCTION

RF cavities pressurized with hydrogen gas are being developed to produce low emittance, high intensity muon beams for muon colliders, neutrino factories, and other applications. The high-pressure gas suppresses dark currents, multipacting, and other effects that are complicating factors in the study of breakdown in the usual RF cavities

that operate in vacuum.

In the studies reported here, various metals were tested in a pressurized cavity where RF breakdown is expected to be due only to the interaction of the metallic surfaces with the electromagnetic fields. After exposure to the RF fields, metallic Be, Mo, Cu, and W samples were examined using a Hirox microscope and a scanning electron microscope (SEM) to measure the distribution of breakdown events on the electrode surfaces.

7.2 APPARATUS

A schematic of the 805 MHz Test Cell (TC) geometry is shown in Fig. 7.2. The TC is a cylindrical stainless steel pressure vessel. RF power is fed into the chamber via a coaxial line. A solenoid magnet (not shown in the figure) provides an axial magnetic field of up to 3 T, which is used in some of the data sets. Replaceable hemispherical electrodes of various materials (Cu, Mo, Be, W) are separated by a 2 cm gap.

Fig. 7.2. Cross section of the test cell showing the replaceable one inch radius Cu, Mo, W, or Be hemispherical electrodes. The top and bottom plates and the cylinder are copper-plated stainless steel (the gas input/exhaust port is not shown in the Fig. 7.2).
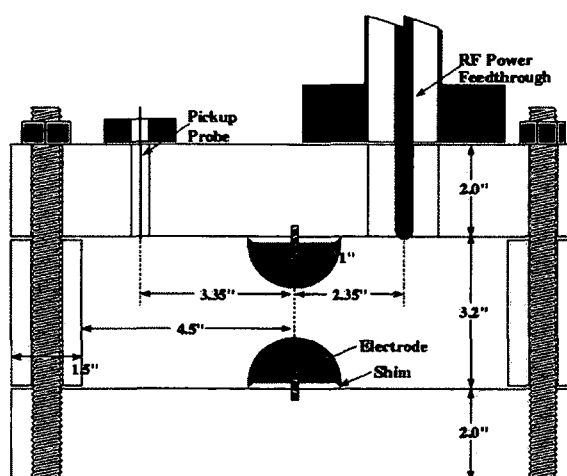
Fig. 7.2. Schematic of the 805 MHz Test cell

7.3   EXPERIMENTAL RESULTS

RF breakdown

Increasing gas density reduces the mean free collision path for ions giving them less chance to accelerate to energies sufficient to initiate showers and avalanches. As shown in Fig. 7.3.1, it is found that Cu and Be electrodes operated stably with surface gradients near 50 MV/m, Mo near 65 MV/m, while W achieved values near 75 MV/m.

Electrode Analysis

After the exposure of the electrodes to acquire the data shown in Fig. 7.3.1, each electrode was examined using secondary and Hirox microscopes. The local surface density of breakdown remnants was recorded as a function of the zenith angle (zero angle corresponds to the axis of the TC). On Be, the breakdown remnants mostly look like boiled melted areas in a tadpole shape with head and tail (Fig. 7.3.2). For Mo the breakdown remnants look like overlapped circular melted regions and some splashed areas. Small holes in the melted region may be vents of metallic vapor due to boiling (Fig. 7.3.3). Tungsten breakdown remnants are furrow-shaped melted areas extended on the surface ending in a series of overlapped circles (Fig. 7.3.4). Cracks that are seen on the breakdown areas are assumed to have occurred subsequent to breakdowns because they are seen on the last ending circle of the set of repeated circles.
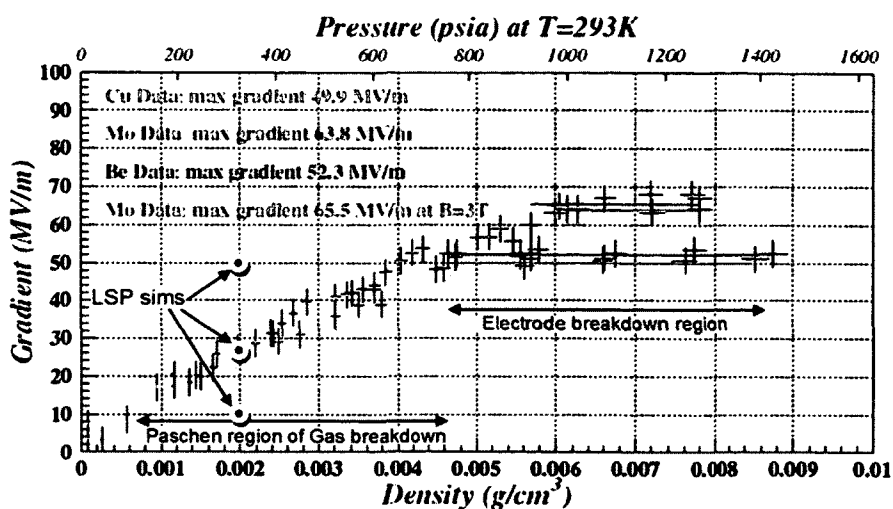
Fig. 7.3.1. Maximum stable TC gradient as a function of hydrogen gas density or pressure for Cu, Be, and Mo with no external magnetic field and Mo with 3 T. The three points labeled "Lsp sims" correspond to simulation results discussed below.

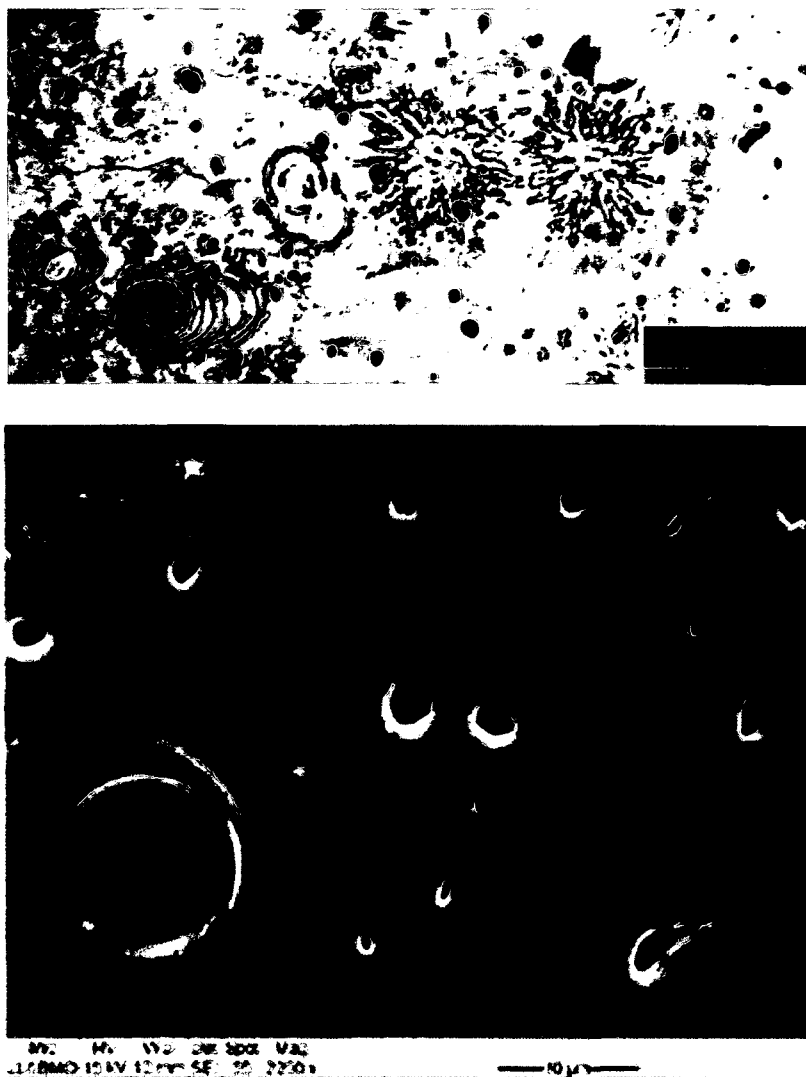Fig. 7.3.2. Beryllium breakdown remnants.
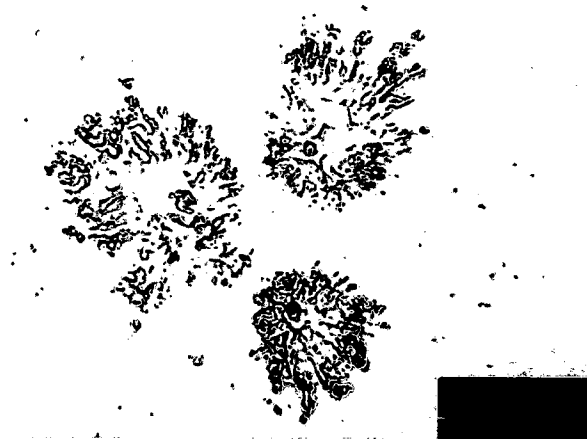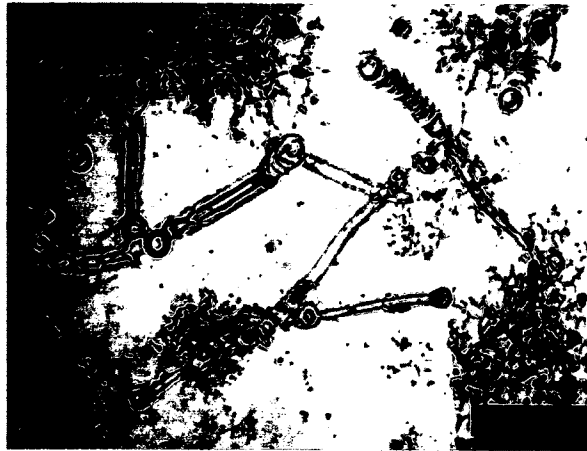
Fig. 7.3.3. Molybdenum remnants.

Fig. 7.3.4. Tungsten Breakdown.

7.4   EXPERIMENTAL DATA ANALYSIS

To investigate the correlation of breakdown and the electric field, the local surface density of breakdown remnants was compared with the maximum expected electric field using an ANSYS model. Least squares fits of the data to a power of the predicted maximum electric gradient at the surfaces of the electrodes show good agreement for high values of the exponent. Fig. 7.4.1 shows the predicted maximum surface gradient (dashed), the data (black with error bars) as described above, and the best least squares fit (red) to the data y=0.34E7 versus zenith angle for Be. Fig.s 7.4.2 and 7.4.3 show the experimental data, the ANSYS model data, and best fits for Mo and W respectively.
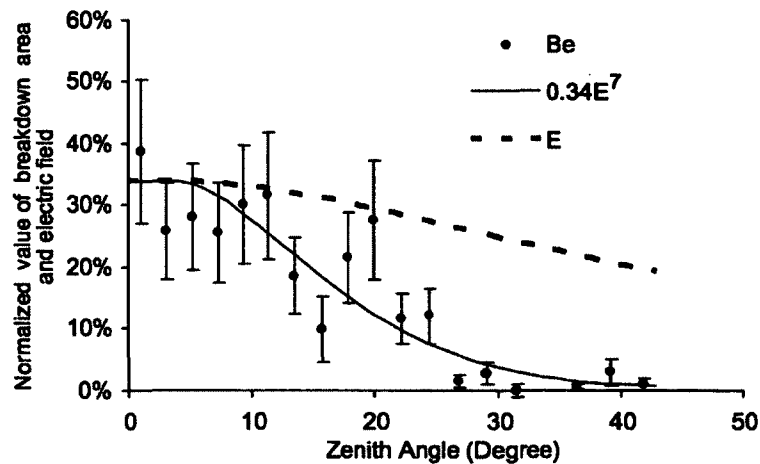

Fig. 7.4.1. Be breakdown area fraction vs. zenith angle.

The plots also show that the breakdown data correlates with a high power of electric field: 7 for Be, 11.5 for Mo and 10 for W. This suggests that the breakdown is a quantum mechanical effect described by the Fowler-Nordheim theory of field emission by tunneling of electrons through a barrier in the presence of a high electric field.

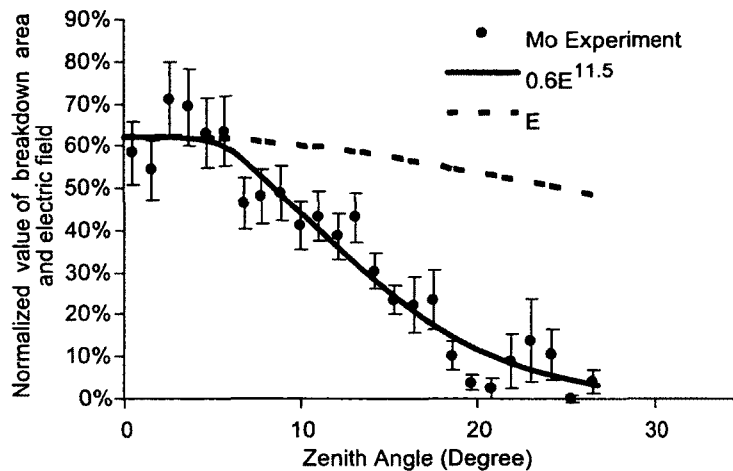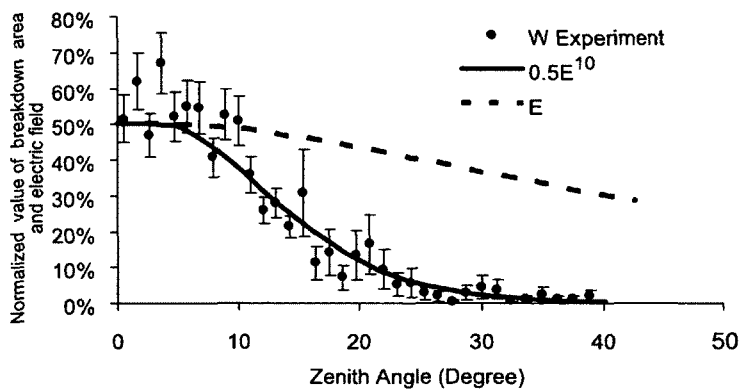Fig. 7.4.2. Mo breakdown area fraction vs. zenith angle.

Fig. 7.4.3. W breakdown area fraction vs. zenith angle.

7.5 FIRST COMPUTER SIMULATION

Computer calculations to simulate the behavior of breakdown in helium-filled spark- gap switches [109] have been extended to use hydrogen in the Muons, Inc. Test Cell [110] Three values of electric field were used for the calculations in the conditions

of Fig. 7.2 at a density of 0.002 g/cm3 as indicated by the three red and blue dots.

Fig. 7.5 shows the simulation results for the three electric filed strengths, where the electron density is stable below the Paschen curve (10 MV/m), slightly unstable at the curve (25 MV/m), and very unstable for values above the curve (50 MV/m).
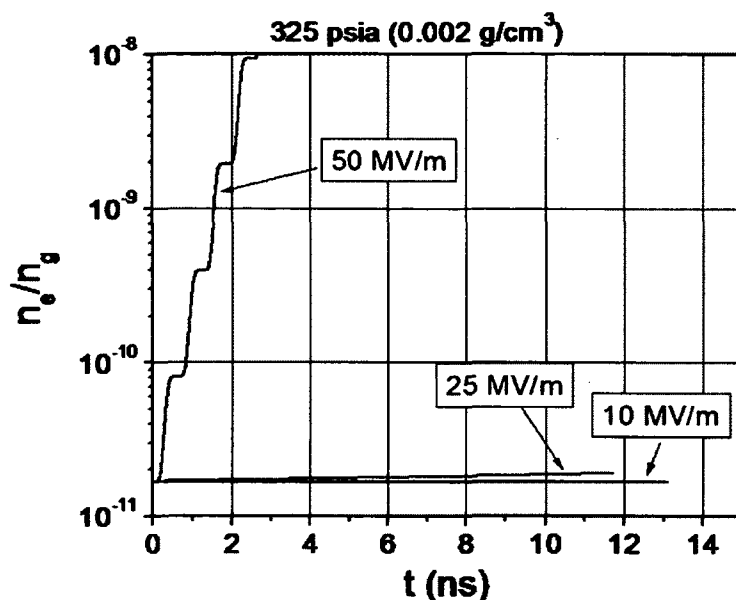
Fig. 7.5. Electron density as a function of time at 805 MHz and gas density 0.002 $g \cdot cm^{-3}$.

The temporal evolution of these curves is consistent with the results of the experiment; for E0 = 10 MV/m, the electron population does not grow because the field is too low to induce ionization of the neutral H2. At 25 MV/m, the electron density is slowly growing, consistent with this value of E0 being at the edge of the Paschen law breakdown limit in Fig. 7.2. At 50 MV/m, the electric field drives electrons in the tail of the distribution to high enough energies to efficiently ionize the gas. It is interesting that the 805 MHz period is seen in the growth of the electron density.

One proposed method to increase the effective breakdown threshold for the gas at a given pressure is to introduce a low concentration of electro-negative gas to the H2. A

very low ratio mixture of SF6 is used to examine this effect. Three additional particle species of neutral SF6, SF+6 , and SF−6 are added to the calculation. The results of a calculation at E_0 = 25 MV/m are shown in Fig. 7.6, which plots the electron and negative ion density as a function of time. The initial electron population rapidly decreases, as the negative ion density increases. This demonstrates the desired effect of increasing the Paschen limit for breakdown in pure H2.

7.6 CONCLUSIONS

The breakdown data shown in Fig.s 7.4.1-3 show good agreement with high powers of electric field. This strong electric field dependence of the breakdown in pressurized gas is so similar to the dark current dependence predicted by Fowler and Nordheim that breakdown of a metal in a strong electromagnetic field is very likely also a quantum mechanical effect. The fact that the conditioned surfaces of the elec- trodes are rougher than the factor in the Fowler-Nordheim expression is not the dominant effect. Thus the work function is a likely factor in the ultimate breakdown limit of metallic structures. This has inspired the study of the distributions of work functions in the electrodes using scanning tunneling microscopy. On another front, computer simulations of the Paschen region of the breakdown data of the Test Cell show good agreement. The next steps to extend the model to include the metallic electrodes may give more insight to the mechanism of RF breakdown.
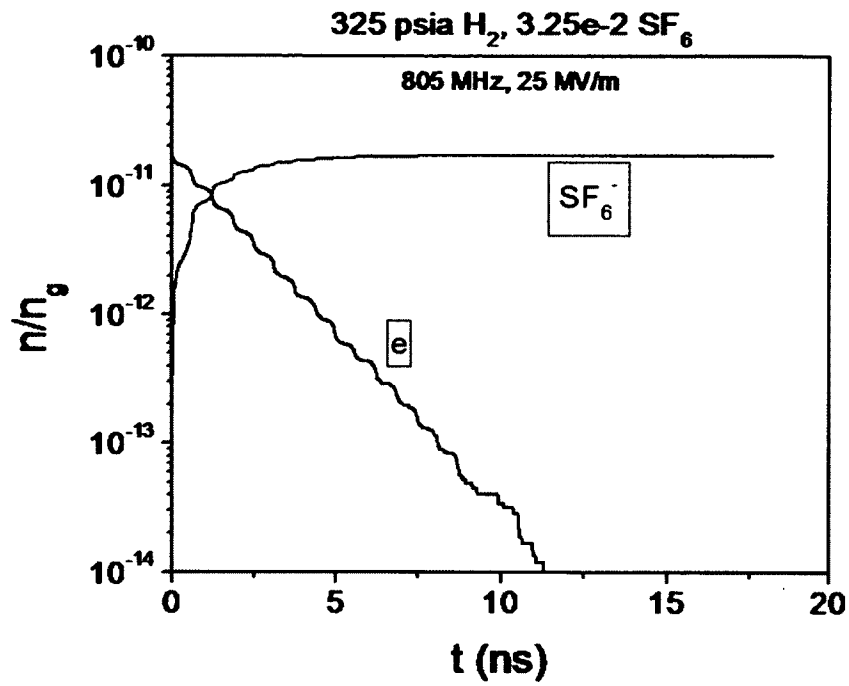
Fig. 7.6. Electron density depletion and SF6 ion density growth as a function of time at H2 density 6 · 1020 cm^{-3} and SF6 density of 6 · 1016 cm^{-3}.

REFERENCES

[1]   J. Rosenzweig, G. Travish, and L. Serafini, World Scientific Publishing Company, Inc. (2004)

[2]   I. V. Bazarov and C. K. Sinclair, Phys. Rev. ST Accel. Beams 8, 034202 (2005)

[3]   I. V. Bazarov, et al. , Phys. Rev. Lett., 102, 104801 (2009)

[4]   C.K.Sinclair, Proceedings of the PAC, 76 (2003)

[5]   K. Aulenbacher, et al., Nucl. Instrum. Methods in Physics Research Section A: Accelerators, Spectrometers, Detectors and Associated Equipment, 391, 498-506 (1997)

[6]   H. G. Andresen, et al., Proc. of Workshop on Photocathodes for Polarized Electron Sources for Accelerators, SLAC (1993)

[7]   C.K. Sinclair, Proceedings of the PAC, New York, NY, (1999)

[8]   E. Pozdeyev, Proceedings of the PAC, Albuquerque, New Mexico, USA (2007)

[9]   I.V. Bazarov, et al., Physical Review Special Topics: Accelerator Beam 11, 040702 (2008)

[10]   R. Hajima and R. Nagai, Nucl. Instrum. Methods Phys. Res. A 557, 103 (2006)

[11]   C. Hernandez-Garcia et al., " Proceedings of the 45th ICFA Advanced Beam Dynamics Workshop, Cornell University, Ithaca, NY, pp. 37–39 (2009)

[12]   L. B. Jones, et al., Proceedings of the 18th International Symposium on High Energy Spin Physics AIP Conf. Proc. No. 1149 p. 1084 (2008)

[13]   B. M. Dunham and K. W. Smolenski, Power Modulator and High Voltage Conference, IEEE International, Atlanta GA, 98-101 (2010)

[14]   N. Nishimori, et al., Proceedings of the 18th International Symposium on High Energy Spin Physics AIP Conf. Proc. No. 1149, p. 1094 (2008)

[15]   C. Hernandez Garcia, et al., Thomas Jefferson National Accelerator Facility, Newport News, VA 23606, "DC High Voltage Conditioning of Photoemission Guns at Jefferson Lab FEL," AIP Conf. Proc. 1149, pp. 1071-1076

[16]   C. K. Sinclair, Nuclear Instruments and Methods in Physics Research A 557 69–74, (2006)

[17]   C. Hernandez-Garcia, et al., 26th. International Free Electron Laser Conference,

Trieste, Italy, 558, (2004)

[18] D.J. Holder, et al., CCLRC Daresbury Laboratory, U.K., "The status of the Daresbury energy recovery prototype project", Proceedings of EPAC, Edinburgh, Scotland (2006)

[19] Y. M. Saveliev, et al., STFC Daresbury Laboratory, ASTeC & Cockcroft Institute, UK, Proceedings of IPAC, New Orleans, Louisiana, USA (2012)

[20] B.M. Dunham, et al., IPAC 2012, New Orleans, Louisiana (May 2012)

[21] K. Smolenski, et al., AIP Conf. Proc. 1149, pp. 1077-1083 (2008)

[22] T. Nishitani, et al., Proceedings of FEL, BESSY, Berlin, Germany (2006)

[23] N. Nishimori, et al., Proceedings of ERL, Daresbury, UK (2007)

[24] L. Merminga, et al., Annu. Rev. Nucl. Part. Sci. 53, 387 (2003)

[25] R.W. Wood, Phys Rev. 5(1), 1(1897)

[26] W. Schottky, Z. Physik 14, 63(1923)

[27] Millikan, R.A and Lauritsen, C.C., Proc. Nat. Acad. Sci.(US), 14, 45-49, (1928)

[28] R. H. Fowler and L. Nordheim, Proc. R. Soc. A 119, 173 (1928)

[29] E. W. Muller, Z. Physik 106, 541 (1937)

[30] E.W. Muller, Z. Physik 108, 668(1938)

[31] R. Haefer, Z. Physik 116, 604(1940)

[32] R.J. Noer, Appl. Phys, A28, 1(1982)

[33] Allen, Cox, Latham, J. Phys D12, 969(1979)

[34] Bayliss, Latham, Proc Royal Soc (London), A403, 285(1986)

[35] N.S. Xu and Latham, J. Phys D19, 477(1986).

[36] R. V. Latham, "High Voltage Vacuum Insulation," Academic Press, London (1995)

[37] N. Pupeter, Dissertation, WUB-DIS 96-16, University of Wuppertal(1996)

[38] E. Mahner, N. Minatti, H. Piel, and N Pupeter, Appl. Surf. Sci.67, 23(1993)

[39] T. Wang, C. E. Reece, and R.M. Sundelin, J. Cac. Sci. Technol. B21, 1230(2003)

[40] A. Dangwal, et al., J. Appl. Phys. 102, (2007)

[41] P. Kniesel, et al., Proc. PAC, Knoxville, Tenessee, p3991(2005)

[42] P. Adderley, et al., Phys. Rev. ST Accel. Beams 13, 010101 (2010)

[43] M.J.J. van den Putte, et al., Methods Phys. Res., Sect. A 406, 50 (1998)

[44] R. Nagai, et al, Rev. Sci. Instrum. 81, 033304 (2010)

[45] F. Furuta et al., Nucl. Instrum. Methods Phys. Res., Sect. A 538, 33 (2005)

[46] C.K. Sinclair et al., Proc PAC, Chicago, IL (2001)

[47] R.H. Fowler, L. Nordheim, Proc. Roy. Soc. A 119, 173 (1928)

[48] R.J. Noer, Appl. Phys, A28, 1(1982)

[49] E. L. Murphy and R. H. Good, Jr., Phys. Rev. 102, 1464 (1956)

[50] R. V. Latham, "High Voltage Vacuum Insulation," Academic Press, London
      (1995)

[51] D. Alpert, D.A. Lee, E.M.Lyman, and H. E. Tomaschke: J. Vac. Sci. Technol. 1,
      35 (1964)

[52] G. Vibrans: MIT Lincoln Lab. Report 353 (1964)

[53] Cranberg, L. , J. Appl. Phys. 23, 518-22, (1952)

[54] Rohrbach, F., CERN Report, 71-5/TC-L, (1971)

[55] Jeans, J.H. , In "Mathematical Theory of Electricity and Magnetism", 5th Edn,
      Cambridge University Press, (1958)

[56] Lobedov, N.N, and skal'skaya, I.P., Sov. Phys.-Tech. Phys., 7, 268-71, (1962)

[57]   C. K. Sinclair, et al., Phys. Rev. ST Accel. Beams 10, 023501 (2007)

[58]   P. Kneisel, Proceedings of the 32nd Advanced ICFA Beam Dynamics Workshop
       on Energy Recovering Linacs, edited by S. Chattopadhay and L. Merminga [Nucl.
       Instrum. Methods Phys. Res., Sect. A, 557 (2006)

[59]   A. M. Wagener and H. R. Arthur, Machine Shop Theory   and Practice (D. Van
       Nostrand Company, New York, 1950)

[60]   Y. Tito Sasaki, "Reducing SS 304/316 hydrogen outgassing to 2×10-15 torr l/cm2
       s", J. Vac. Sci. Technol. A 25, 1309 (2007)

[61]   K. Smolenski et al., AIP Conf. Proc. 1149, pp. 1077-1083 (2008)

[62]   R. Nagai et al., Rev. Sci. Instrum. 81 033304 (2010)

[63]   http://www.ableelectropolishing.com

[64]   K. Halbach, Lawrence Livermore National Laboratory Technical Report No.
       UCRL-17436, (1967)

[65]   E. M. Lyman, at al., Proc. II-DEIV, pp.33 -39 (1966)

[66]   Alpert, D., et al., J. Appl. Phys. , 38, 880-1 , (1967)

[67]   Beukema, G.P., J. Phys. D: Appl. Phys., 7, 1740-55, (1974)

[68]   C. S. Athwal and R. V. Latham, Physica C., **104**, pp.189 -195 (1981)

[69]   Ph. Niedermann, et al., J. Appl. Phys., **59**, pp. 892-901(1986)

[70]   R. V. Latham, Vacuum, **32**, pp.137 -140 (1982)

[71]   K. H. Bayliss and R. V. Latham, " Proc. Roy. Soc., 403, pp.285 -311 (1986)

[72]   S. Bajic and R.V. Latham, J. Phys. D. : Appl. Phys. , **21**, pp. 943-950 (1988)

[73]   S. Bajic, at al., IEEE Transactions on electrical Insulation, **24**, No.6 (1989)

[74]   M. Reiser, "Theory and Design of Charged Particle Beams," John Wiley & Sons, Inc., New York, (1994)

[75]   Kieffer et al., J. Reviews of Modern Physics, **38**, Issue 1, pp. 1-35 (1966)

[76]   M. BastaniNejad, et al. , Phys. Rev. STAB, **15**, 083502 (2012)

[77]   Nitrogen equivalent pressure, absolute pressure values for He and Kr should be adjusted by a factor specified by the gauge vendor

[78]   James Biersack, J.P. Ziegler, M.D. Ziegler, "The Stopping and Range of Ions in Matter" (1985)

[79]   Jon Orloff, "Handbook of Charged Particle Optics", CRC Press; 2nd edition (October 24, 2008)

[80]   O.Y. Kolesnychenko, O.I Shklyarevskii, and H. van Kempen, Physica B, **284**, pp. 1257-1258 (2000)

[81]   F. Furuta et al. Nucl. Instrum. and Meth. A 538, 33 (2005)

[82]   B. Bhushan, et al., Ultramicroscopy 89, 39 (2001)

[83]   L. Nilsson, O. Groening, C. Emmenegger, O. Kuettel, E. Schaller, L. Schlapbach, H. Kind, J.-M. Bonard, and K. Kern, Appl. Phys. Lett. 76, 2071 (2000)

[84]   I.V. Bazarov, et al., Physical Review Special Topics: Accelerator Beam 11, 040702 (2008)

[85]   R. Hajima and R. Nagai, Nucl. Instrum. Methods Phys. Res. A **557**, 103 (2006)

[86]   C. Hernandez-Garcia et al., Proceedings of the 45th ICFA Advanced Beam Dynamics Workshop, Cornell University, Ithaca, NY, pp. 37–39 (2009)

[87]   L. B. Jones, S. P. Jamison, Y. M. Saveliev, K. J. Middleman, and S. L. Smith, Proceedings of the 18th International Symposium on High Energy Spin Physics

AIP Conf. Proc. No. 1149 p. 1084 (2008)

[88]   B. M. Dunham and K. W. Smolenski, Power Modulator and High Voltage Conference, IEEE International, Atlanta GA, 98-101 (2010)

[89]   N. Nishimori, R. Nagai, H. Iijima, Y. Honda, T. Muto, M. Kuriki, M. Yamamoto, S. Okumi, T. Nakanishi, and R. Hajima, in Proceedings of the 18th International Symposium on High Energy Spin Physics AIP Conf. Proc. No. 1149, p. 1094 (2008)

[90]   C. Hernandez Garcia, S. V. Benson, G. Biallas, D. Bullard, P. Evtushenko, K. Jordan, M. Klopf, D. Sexton, C. Tennant, R. Walker, and G. Williams, Thomas Jefferson National Accelerator Facility, Newport News, VA 23606, AIP Conf. Proc. 1149, pp. 1071-1076

[91]   BastaniNejad, et al., Phys. Rev. STAB, 15, 083502 (2012)

[92]   W. D. Owen, M. H. Davies, and W. D. Powell, Proceedings of the 3rd International Symposium on Discharges and Electrical Insulation in Vacuum, Paris, pp 163-70 (1968)

[93]   D W Williams and W T Williams, "Effect of electrode surface finish on electrical breakdown in vacuum", J. Phys. D: Appl. Phys. 5 (1845)

[94]   Y. Tito Sasaki, "Reducing SS 304/316 hydrogen outgassing to 2×10-15 torr l/cm2 s", J. Vac. Sci. Technol. A 25, 1309 (2007)

[95]   K. Smolenski et al., AIP Conf. Proc. 1149, pp. 1077-1083 (2008)

[96]   R. Nagai et al., Rev. Sci. Instrum. 81 033304 (2010)

[97]   http://www.ableelectropolishing.com

[98]   C. K. Sinclair, et al., Phys. Rev. ST Accel. Beams 10, 023501 (2007)

[99]   B. Bhushan, et al., Ultramicroscopy 89, 39 (2001)

[100]   R. V. Latham, High Voltage Vacuum Insulation (Academic Press, London, 1995)

[101]   Chen Xu, et al., "Topographic power spectral density study of the effect of surface treatment processes on niobium for superconducting radio frequency accelerator cavities", Phys. Rev. ST Accel. Beams 15, 043502 (2012)

[102]   Hui Tian, et al., "A novel approach to characterizing the surface topography of niobium superconducting radio frequency (SRF) accelerator cavities", Applied Surface Science, 257, Issue 11, 4781–4786 (2011)

[103] James Biersack, J.P. Ziegler, M.D. Ziegler, "The Stopping and Range of Ions in Matter" (1985)

[104] Gruszka and Moscicka-Grzesiak, "Conditioning process of electropolished electrodes by field emission current in vacuum", IEEE Trans. Electr. Insul., EI-20, 4, 705 – 708 (1985)

[105] C. Hernandez Garcia, et al., "DC High Voltage Conditioning of Photoemission Guns at Jefferson Lab FEL", AIP Conf. Proc. 1149, pp. 1071-1076

[106] P. Hanlet, et al., Proceedings of EPAC, Edinburgh, Scotland, p. 1364 (2006)

[107] M. BastaniNejad et al., in Proceedings of PAC07, Albuquerque, New Mexico, p. 2499 (2007)

[108] Lsp is a software product developed by ATK Mission Research, Albuquerque, NM 87110.

[109] C. Thoma, et al. IEEE Trans. Plasma Sci. 34, 910 (2006)

[110] D. V. Rose, C. Thoma, D. R. Welch, and R. E. Clark, Low Emittance Muon Collider Workshop, Fermilab (2008)